

Revealing the proton slingshot mechanism in solid acid electrolytes through machine learning molecular dynamics

Menghang Wang,¹ Jingxuan Ding,¹ Grace Xiong,² Ni Zhan,³ Cameron J. Owen,⁴ Albert Musaelian,¹ Yu Xie,¹ Nicola Molinari,^{1,5} Ryan P. Adams,³ Sossina Haile,² and Boris Kozinsky*,^{1,5}

¹*Harvard John A. Paulson School of Engineering and Applied Sciences,
Harvard University, Cambridge, MA 02138, USA*

²*Materials Science and Engineering, Northwestern University, Evanston, IL 60208, USA*

³*Department of Computer Science, Princeton University, Princeton, NJ 08544, USA*

⁴*Department of Chemistry and Chemical Biology,
Harvard University, Cambridge, MA 02138, USA*

⁵*Robert Bosch Research and Technology Center, Watertown, MA 02472, USA*

ABSTRACT

In solid acid solid electrolytes CsH_2PO_4 and CsHSO_4 , mechanisms of fast proton conduction have long been debated and attributed to either local proton hopping or polyanion rotation. However, the precise role of polyanion rotation and its interplay with proton hopping remained unclear. Nanosecond-scale molecular dynamics simulations, driven by equivariant neural network force fields, reveal a nuanced proton slingshot mechanism: protons are initially carried by rotating polyanions, followed by O–H bond reorientation, and the combined motion enables long-range jumps. This challenges the conventional revolving paddlewheel model and reveals significant independent proton motion that is assisted by limited rotations. Despite structural similarities, we identify qualitative differences in transport mechanisms between CsH_2PO_4 and CsHSO_4 , caused by different proton concentrations. CsH_2PO_4 exhibits two distinct rates of rotational motions with different activation energies, contrasting with CsHSO_4 's single-rate behavior. The higher proton concentration in CsH_2PO_4 correlates with frustrated PO_4 polyanion orientations and slower rotations compared to SO_4 in CsHSO_4 . Additionally, we reveal a correlation between O-sharing and proton transport in CsH_2PO_4 , a unique feature due to extra proton per polyanion compared to CsHSO_4 . Our findings suggest that reducing proton concentration could accelerate rotations and enhance conductivity. This work provides a unified framework for understanding and optimizing ionic mobility in solid-acid compounds, offering new insights into the interplay between proton hopping and disordered dynamics in polyanion rotation.

I. INTRODUCTION

Several solid acid compounds exhibit high proton conductivity as a result of structural disorder [1]. In addition to high ionic conductivity, these compounds typically display negligible electronic conductivity, anhydrous proton transport, and impermeability to fuels, rendering solid acids attractive as electrolytes in a range of electrochemical energy technologies [2, 3]. Technological development efforts have focused on CsH_2PO_4 (cesium dihydrogen phosphate, CDP) due to its stability under both oxidizing and reducing conditions [3, 4]. The material has been demonstrated in pre-commercial fuel cell stacks [5], in hydrogen electrochemical pumps [6], and in ammonia electrolysis cells for on-site production of high purity hydrogen [7].

The essential structural features that result in high conductivity in CsH_2PO_4 and related compounds such

as CsHSO_4 (cesium hydrogen sulfate, CHS) have been under investigation for several decades, ever since the discovery of the spectacular (several orders of magnitude) increase in conductivity at the transition to the disordered state [8, 9]. In a general sense, proton transport is thought to occur via a combination of mechanisms involving local proton hops along O–H...O bonds and rotation of the XO_4 polyanion group (X = P, S, As, Se, etc.) [10, 11]. Molecular dynamics (MD) simulations revealed that at ambient temperature, the structures, which typically crystallize with monoclinic lattice symmetry, lack polyanion rotation. At higher temperatures, the superprotonic phases of CsH_2PO_4 and CsHSO_4 , characterized by cubic ($\text{Pm}\bar{3}\text{m}$) and tetragonal ($\text{I4}_1/\text{amd}$) symmetries, respectively, exhibit rapid polyanion rotation [12, 13].

In the superprotonic phases of CsH_2PO_4 and CsHSO_4 (Figure 1a,b), the number of crystallographically equivalent oxygen sites exceeds the number of oxygen atoms available to fill them, a feature that is suggestive of orientational disorder of the lattice of PO_4 and SO_4 polyanions. The occurrence of polyanion rotation in these structures has been directly observed by

* Corresponding authors

B.K., E-mail: bkoz@g.harvard.edu

nuclear magnetic resonance (NMR) techniques [14–16], quasielastic neutron scattering (QENS) [14, 17], measurements of dielectric relaxation [18], and MD studies [12, 13, 19, 20]. Therefore, rapid polyanion rotation has long been recognized as the key contributor to fast proton mobility.

Significantly, these studies have suggested that the rate limiting mechanism for proton motion in superprotonic CsH_2PO_4 and CsHSO_4 differ. Specifically, polyanion rotation has been hypothesized as rate-limiting in CsH_2PO_4 , while local proton hopping is rate-limiting in CsHSO_4 . However, these hypotheses and observations have remained qualitative, considering local proton hopping and polyanion rotation as independent steps, neglecting correlations between them. Our goal is to examine the possible interplay between the two mechanistic steps, with the use of long timescale simulations, and to quantitatively capture the polyanion dynamics that directly influence proton trajectories, particularly identifying which types of rotations facilitate and control long-range proton diffusion.

Meanwhile, the precise contribution of polyanion rotation in proton transport remains unclear. Specifically, it is debated whether large-angle rotations are necessary or if small-scale rotations suffice for proton transfer in solid acid compounds, as short *ab initio* molecular dynamics (AIMD) simulations have not observed large tumbling motions [19, 20]. Clarifying the magnitude of polyanion rotations required for effective proton transport is crucial to understand the conduction mechanism.

The relationship between proton concentration and XO_4 rotation rates in CsH_2PO_4 and CsHSO_4 remains unexplored. Previous ^{17}O NMR studies on monoclinic CsH_2PO_4 demonstrated improved agreement between simulations and experimental observations when considering two distinct PO_4 rotation rates, yet this phenomenon lacks thorough investigation in superprotonic phases of both compounds. Recent findings also challenge conventional understanding: the proton-excess compound $\text{Cs}_7(\text{H}_4\text{PO}_4)(\text{H}_2\text{PO}_4)_8$ exhibits lower conductivity than superprotonic CsH_2PO_4 [22], contrary to expectations that higher proton concentration enhances conductivity. Additionally, observed differences in rotation rates between H_4PO_4^+ polycations and H_2PO_4^- polyanions [23] highlight the need to understand how local proton coordination affects rotation dynamics.

Investigating coupled polyanion dynamics and proton transport mechanisms faces significant computational constraints. Traditional AIMD simulations are limited to 200 atoms and 250 picoseconds [12], preventing observation of long-timescale mechanistic coupling. Accurate modeling of polyanion orientational disorder in the superprotonic phase demands larger systems to minimize finite size effects [20]. Moreover, to capture

statistically significant proton diffusion events, AIMD simulations require temperatures beyond the thermal stability limits of CsH_2PO_4 and CsHSO_4 .

Machine learning force fields (MLFFs) significantly expand the scope of MD simulations while preserving *ab initio* accuracy [24–28]. After learning the mapping from atomic geometries to forces calculated by density functional theory (DFT), a MLFF predicts forces at each MD update step, replacing DFT calculations during simulation. This enables the study of dynamics on longer timescales and larger system sizes than traditional AIMD. Recent applications to proton-conducting media containing phosphoric acid [13, 29] have revealed the intricate interplay between polyanion rotation and proton bonding, with Minami *et al.* demonstrating that hydrogen bond recombination promotes polyanion rotations [29]. These findings suggest that proton transport mechanisms extend beyond the traditional two-step process.

In this work, we leverage our recently developed MLFF techniques to quantitatively understand and discover new details of the proton conduction mechanisms in the superprotonic phases of CsH_2PO_4 and CsHSO_4 . Through nanosecond simulations of thousands of atoms with *ab initio* precision, we reveal a novel slingshot transport mechanism, where synchronized polyanion rotation and O–H bond reorientation control long-range proton diffusion. In CsH_2PO_4 , we discover two distinct polyanion rotation rates with different activation energies, correlated with local proton coordination fluctuations. The higher proton concentration in CsH_2PO_4 leads to frustrated polyanion orientations, contrasting with CsHSO_4 where SO_4 polyanions exhibit preferential orientations near those observed in neutron diffraction studies [21]. By uncovering the coupled mechanisms of polyanion rotation, O–H bond reorientation, and local proton coordination, these findings provide foundational insights for designing next-generation solid-state electrolytes with enhanced performance.

II. METHOD

Our investigation is made possible by an accurate and reliable MLFF capable of capturing ion dynamics over long timescales. We trained the equivariant MLFF Allegro [28] on a diverse dataset of structures with corresponding DFT energies and forces, collected through the Bayesian active learning framework FLARE [25, 26, 30].

DFT calculations were performed with the Perdew-Burke-Ernzerhof (PBE) [33] functional, which accurately describes material properties in both monoclinic phases [34, 35] and superprotonic phases [12, 19, 20, 36, 37] of CsH_2PO_4 and CsHSO_4 . Calculations were executed

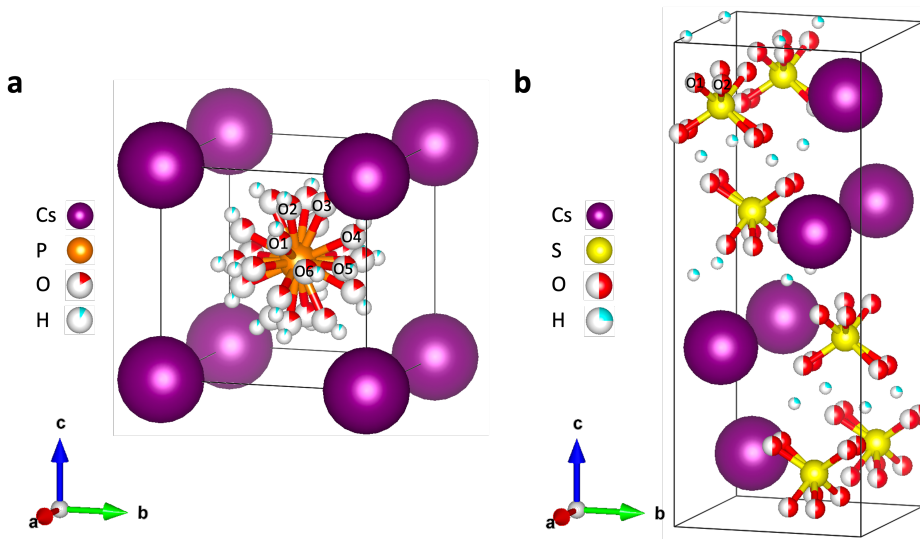


Figure 1. Superprotonic structures. The superprotonic phase of (a) CsH_2PO_4 [15] and (b) CsHSO_4 [21]. The oxygen sites in CsH_2PO_4 have a one-sixth average occupancy, whereas those in CsHSO_4 have a one-half average occupancy. Both PO_4 and SO_4 polyanions are orientationally disordered. The H position in CsH_2PO_4 is determined according to [20], with details provided in Supporting Information.

using the Vienna *ab initio* simulation package (VASP) [38–40], with detailed DFT parameters provided in Supporting Information.

Diverse training data is essential for stable MLFFs. While short AIMD trajectories often fail to capture varied polyanion orientations and rare proton jump events, FLARE automates data collection and ensures data diversity. FLARE employs rotationally invariant B2 descriptors from the atomic cluster expansion (ACE) [41] to describe atomic environments and uses sparse Gaussian processes (SGP) [25] to construct a Bayesian force field (BFF). The BFF predicts atomic forces and uncertainties on local atomic environments during an active learning MD simulation. When uncertainties exceed a set threshold, FLARE invokes DFT calculations to calculate interatomic forces, energy, and stresses for the MD snapshot and updates both the training set and the SGP model.

The dataset generation, shown in Figure 2a, consists of multiple active learning trajectories covering varying temperatures, pressures, and supercell sizes for superprotonic and monoclinic phases, each initiated with an empty SGP model. Each compound’s dataset was split into training (80%), validation (10%), and test (10%) sets, maintaining proportional representation across different active learning trajectories. This dataset forms the foundation for training the Allegro MLFF. Further details on dataset generation are described in Supporting Information.

Neural network-based MLFFs often yield higher accuracy than models based on hand-crafted descriptors, though challenges in efficiency and robustness persist.

Equivariant MLFFs [27, 28], such as Allegro [28], have shown low error, high sample efficiency, and robustness across various materials. Allegro combines symmetry-invariant and equivariant features using tensor products, depicted in Figure 2a, in a deep equivariant graph neural network, achieving superior accuracy and robustness compared to models using only invariant information [42].

We trained two Allegro MLFFs using identical architectures, one on the CsH_2PO_4 dataset and one on the CsHSO_4 dataset. Each model consists of 2 layers with 32 features under irreducible representations of $O(3)$ symmetry group and a l_{\max} of 2. The 2-body latent multi-layer perceptron (MLP) consists of three layers of dimension [32, 64, 128], using SiLU nonlinearities in the hidden layers. The later latent MLPs consist of two hidden layers of dimension [128, 128]. The final MLP has the dimension of 32 and no nonlinearity. MLPs were initialized with a uniform distribution of unit variance. We applied a radial cutoff of 7.0 Å for local atomic environments.

Each model was trained using a joint loss function combining the mean square error of energies and forces:

$$\mathcal{L} = \frac{\lambda_E}{B} \sum_b \left(\hat{E}_b - E_b \right)^2 + \frac{\lambda_F}{3BN} \sum_i \sum_{\alpha=1}^3 \left\| -\frac{\partial \hat{E}}{\partial r_{i,\alpha}} - F_{i,\alpha} \right\|^2 \quad (1)$$

where B is the batch size, N is the number of atoms, E_b, \hat{E}_b are the true and predicted energies of a given batch, and $F_{i,\alpha}$ is the force component on atom i in direction α . Energy and force losses were weighted equally with $\lambda_E = 1$ and $\lambda_F = 1$. We applied a learning

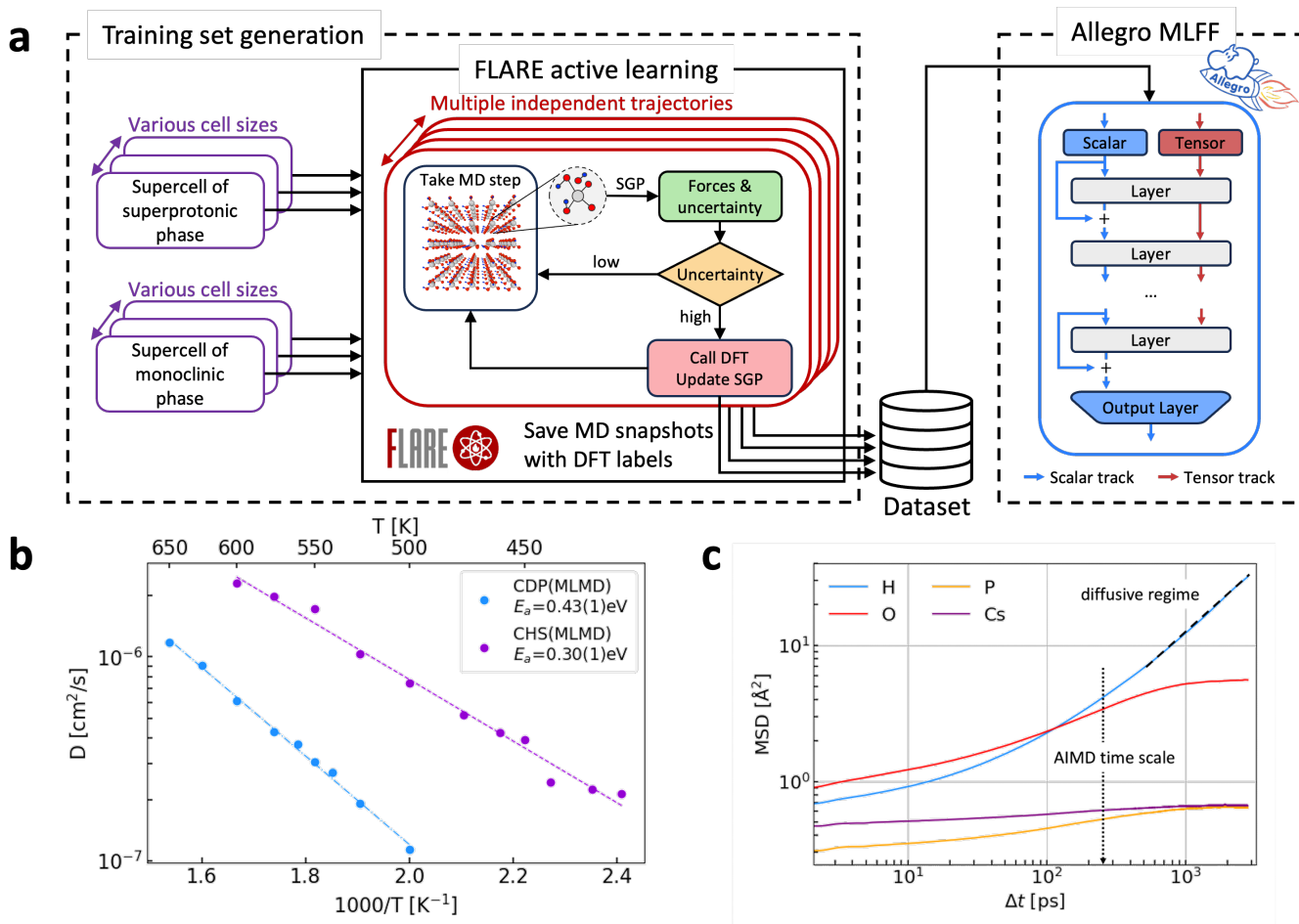


Figure 2. MLFF workflow, diffusion coefficients, and MSD. (a) Left: workflow overview for generating training data of high diversity using FLARE Bayesian active learning [26, 30]. Right: Allegro equivariant MLFF architecture [28]. (b) For CsH₂PO₄ (CDP), the proton diffusion activation energy from ML MD is 0.43(1) eV, consistent with experimental values of 0.39 [14] to 0.43 eV [31]. For CsHSO₄ (CHS), the activation energy from ML MD is 0.30(1) eV, also in agreement with experimental values ranging from 0.29 [16] to 0.36 eV [32]. (c) MSD of each species in CsH₂PO₄ from a 4 ns ML MD at 525 K. Typical AIMD simulations have not yet reached the proton diffusive regime (dashed line).

rate of 0.002 and a batch size of 5, using the Adam optimizer [43] in PyTorch [44], with default parameters ($\beta_1 = 0.9$, $\beta_2 = 0.999$, $\epsilon = 10^{-8}$, no weight decay).

We used an on-plateau scheduler, with a patience of 50 and a decay factor of 0.8, reducing the learning rate based on the validation loss. An exponential moving average with a weight of 0.99 was used for evaluation on the validation set and the final model. All models were trained with float32 precision on a single NVIDIA A100 GPU.

The mean absolute errors on test sets are 0.64 and 1.6 meV/atom in energy, and 31 and 56 meV/Å in forces for CsH₂PO₄ and CsHSO₄, respectively. The force parity plots (Figure S1, Supporting Information) demonstrate excellent agreements between Allegro predictions and DFT-calculated forces. To evaluate robustness, we

varied cell parameters in the superprotonic phases to predict the equation of state of both compounds. Even for cell volumes outside the training set, Allegro achieved predictive errors within 2 meV/atom (Figure S2, Supporting Information).

We use the trained Allegro MLFF to drive MD simulations of the superprotonic phase under the NVT ensemble at temperatures above the superprotonic transition via LAMMPS [45]. The simulation cell contains 1,000 atoms for CsH₂PO₄ and 1,344 atoms for CsHSO₄. Each trajectory runs for 3 or 4 ns with a 0.5 fs time step to accurately simulate proton dynamics. We save ML MD snapshots every 50 fs and equilibrate the system for 10 ps before analyzing the dynamics. Superprotonic phase MD simulations used experimental unit cell parameters: 4.95 Å for CsH₂PO₄ (Pm3m) [15]

and $a = b = 5.72 \text{ \AA}$, $c = 14.23 \text{ \AA}$ for CsHSO_4 ($I4_1/amd$) [21]. These unit cells were duplicated to construct simulation supercells. See Supporting Information for details.

III. RESULTS

The methodological framework described above enables nanosecond-scale MD simulations essential for investigating proton transport mechanisms. Here, we first analyze diffusion characteristics and activation energies of both compounds.

A. Diffusion coefficients and activation energies

In Figure 2c, the mean square displacement (MSD) of protons in CsH_2PO_4 shows that a fully diffusive regime (following Fick’s law, $\alpha = 1$ for $\text{MSD}(\text{H}) \sim (\Delta t)^\alpha$) is reached only after about 500 ps. Meanwhile, the oxygen MSD reaches a plateau after 1 ns, implying that nanosecond long MD is necessary to fully explore the polyanion configurations. Similarly, the MSD plot of CsHSO_4 (Figure S3, Supporting Information) shows that equilibration timescales above 200 ps are needed to reach the proton diffusive regime. These results suggest that previous AIMD simulations only elucidated proton dynamics before reaching the diffusive regime, thus insufficient to capture the transport mechanisms or predict diffusivity.

We validate our ML MD simulations by comparing computed proton diffusion coefficients and Arrhenius activation energies with experimental measurements. Our ML MD-derived diffusion coefficients show significantly better agreement with experiments compared to previous AIMD studies, which deviated by an order of magnitude [12, 19, 20]. The calculated activation energies of 0.43(1) eV for CsH_2PO_4 and 0.30(1) eV for CsHSO_4 (Figure 2b) closely match experimental values [14, 16, 31, 32], with uncertainties derived from linear Arrhenius fits. While our simulations accurately capture the activation barriers, they predict twice the proton conductivity in CsHSO_4 compared to CsH_2PO_4 , contrary to experimental observations of similar conductivities [46]. Detailed methodology for diffusion coefficient calculations and error analysis is provided in Supporting Information.

B. Two types of rotational motions

Building on the finding that overall proton transport properties are accurately predicted by our ML MD simulations and agree with experiments, we proceed

to investigate the mechanistic relationship between polyanion rotations and proton transport.

For every proton, we track its nearest O neighbor and observe that the proton rapidly hops between a pair of O anions belonging to different PO_4 polyanions (Figure 3d). This process, which we refer to as proton rattling, occurs at characteristic timescales of 0.27 ps for CsH_2PO_4 at 525 K and 2.3 ps for CsHSO_4 at 450 K, consistent with previous AIMD studies of solid acids [12, 19, 20]. However, rattling motions do not directly contribute to long-range transport, as protons remain confined within the same O-pair, where both O atoms are covalently bonded to immobile P atoms. Figure 3c demonstrates that rattling produces only minor fluctuations in proton displacement.

Beyond rattling timescales, protons experience O-pair changes (Figure 3d) through two distinct polyanion rotation mechanisms. In **nonproductive exchanger rotation** (Figure 3a), the exchanger polyanion rotates counterclockwise, breaking the $\text{H}\cdots\text{O1}$ bond, while the carrier polyanion maintains the O2-H bond until proton transfer to O3. Although this changes the proton’s O-pair from (O2, O1) to (O2, O3), it remains within the same polyanion pair (P-pair), producing minor displacement and no long-range transport.

In **productive carrier rotation** (Figure 3b), significant proton displacement occurs through “P-pair switches” (red dashed lines, Figure 3c,d,e). The carrier polyanion’s substantial rotation transports the proton from a provider to a recipient polyanion, changing the P-pair from (P1, P2) to (P1, P3). This three-polyanion mechanism enables long-range proton diffusion.

We note that QENS and NMR experiments observe two types of protonic motions: a librational one with distance of 0.8 Å and a translational jump of 2.7 Å [14], which validates our finding. However, previous computational studies [12, 19, 20] did not distinguish between these motions, due to limited statistics from AIMD data.

Having identified these distinct rotation types, we now analyze their characteristics by measuring the displacement of proton-bonded O anions during the rotation period $[t_s, t_f]$. The O displacement during rotation is quantified from onset (t_s) to completion (t_f) using Eq. 2:

$$\Delta r_{\text{O}} = |\mathbf{r}_{\text{O}}(t_f) - \mathbf{r}_{\text{O}}(t_s)|, \quad (2)$$

where t_s marks the proton’s formation of O–H bond with the carrier polyanion and t_f indicates the breaking of this O–H bond and return to proton rattling. For the exchanger polyanion, we measure the displacement of the target oxygen (O3 in Figure 3a), which shares the same PO_4 tetrahedron with O1. The rotation axis is defined by the normal vector to the plane swept by the P–O vector during $[t_s, t_f]$. These rotations typically complete

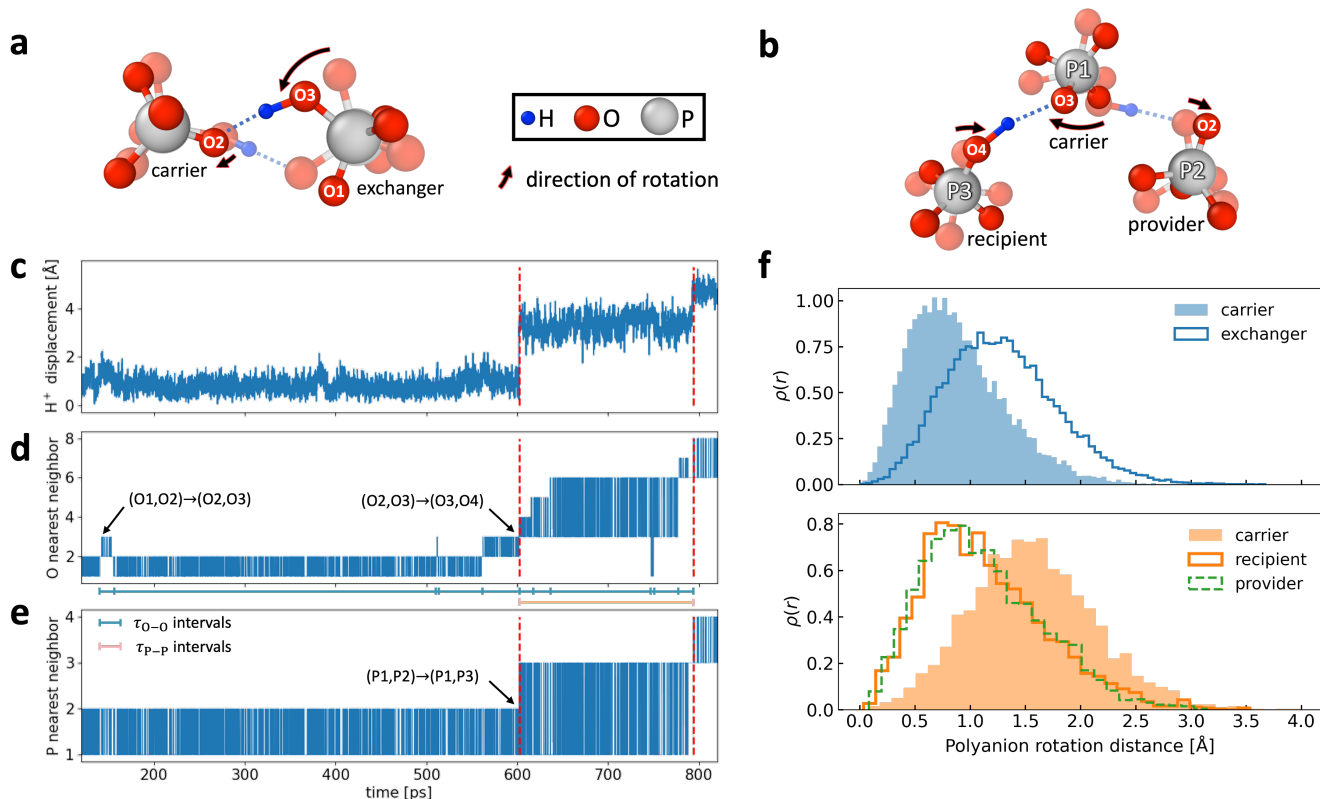


Figure 3. Single proton trajectory and two types of polyanion rotations. Illustration of two types of polyanion rotation for a given proton: (a) Nonproductive exchanger rotation: the proton resides in the same pair of polyanions after the breaking of O–H···O bond; (b) Productive carrier rotation: the proton is transferred to a new polyanion assisted by a carrier rotation and experiences a significant long-range motion, labeled by vertical red dashed lines. For both rotation types, the carrier maintains the O–H bond during the rotation. An excerpt of a single proton trajectory from a ML MD of CsH_2PO_4 at 525 K including: (c) Proton displacement relative to $t = 0$. The rapid change of the nearest oxygen neighbor indicates proton rattling within an O-pair. (d) Time evolution of the index of the nearest O neighbor. (e) Time evolution of the index of the P atom defining the PO_4 polyanion containing the nearest O. (f) Histogram of rotation distances in carrier and exchanger polyanions during nonproductive exchanger rotation (top) compared to those in carrier, recipient, and provider polyanions during productive carrier rotations (bottom).

within picoseconds (Figure S5, Supporting Information), highlighting the rapid nature of proton hopping.

Histograms in Figure 3f reveal that productive rotations involve greater carrier movements than nonproductive ones, highlighting the importance of significant carrier rotation for long-range proton hopping. Within productive rotations, the carrier rotates more than other polyanions, whereas in nonproductive rotations, the exchanger exhibits more rotation.

Notably, no large scale rotation occurs during long-range proton diffusion. The mean distance of productive carrier rotation is 1.6 Å, corresponding to an approximate 61° rotation of the P–O bond between t_s and t_f . This is less than the 109.5° between adjacent P–O bonds in a PO_4 tetrahedron, supporting the hypothesis that extensive PO_4 rotation is not required for proton transfer

in CsH_2PO_4 [20]. Nevertheless, this carrier rotation distance is less than the 2.7 Å proton jump observed via NMR [14]. While recipient rotation (peak at 0.7 Å) may narrow the gap across proton sites, it does not fully explain the jump distance. Therefore, while polyanion rotation facilitates proton jump, the complete jump likely involves O–H bond reorientation, as further discussed in section III F.

C. Independence of rotational dynamics

Given the significant magnitude of nonproductive exchanger rotations, we question whether they participate in productive rotations for other protons. Specifically, we exam temporal overlaps between

rotation periods of these processes (details in Supporting Information).

Analysis reveals that nonproductive rotations operate largely independently of productive transport: 94% of nonproductive exchanger rotations and 98% of nonproductive carrier rotations show no temporal overlap with productive rotations of the same polyanion (Table S2, Supporting Information). The slightly higher non-overlap probability for nonproductive carrier rotations may arise from their smaller rotation magnitude. These results suggest that nonproductive rotations play a limited role in productive processes.

D. Rates and energy barrier of rotations

To estimate rotation rates, we track each proton's residence times in O-pairs (τ_{O-O} intervals) and P-pairs (τ_{P-P} intervals), as illustrated in Figure 3d,e. O-pair residence times measure intervals between all rotations (productive and nonproductive), while P-pair residence times capture only intervals between productive rotations.

Leveraging large-scale ML MD simulations, we obtain sufficient statistics of proton residence time distributions (Figure 4a). Our analysis reveals that τ_{O-O} follows a two-rate exponential distribution, while τ_{P-P} fits a single-rate exponential distribution on a log-linear scale. Fitting these distributions $\rho(\tau)$ yields robust average rates, enabling us to distinguish activation energies of productive rotations from those of combined productive and nonproductive processes. Previous studies were limited to NMR measurements of activation energies in the monoclinic phase [47], while MD simulations [12, 13, 19] provided only qualitative insights through P-O bond vector decorrelation times (Eq. 5). Our ML MD analysis extends quantitative mechanistic understanding to the superprotonic phase, identifying the activation barriers for productive rotations.

The exponential distributions (Figure 4a) indicate that rotation events are independent and follow a Poisson process. The τ_{O-O} distribution exhibits two distinct rates at 525 K in CsH_2PO_4 : a fast rate ($\lambda_1 = 1/21 \text{ ps}^{-1}$) and a slow rate ($\lambda_2 = 1/154 \text{ ps}^{-1}$), with transition at characteristic time $\tau_c = 72 \text{ ps}$. Both nonproductive and productive rotations display this two-rate behavior (Figure S4, Supporting Information), suggesting fast and slow rotations are intrinsic properties independent of rotation type. The τ_{P-P} distribution mainly follows a single rate ($\lambda_3 = 1/499 \text{ ps}^{-1}$) at long time scales, representing the frequency of productive rotations. These rates provide a proton-centric view of rotation dynamics through O-pair and P-pair switches (additional details of the statistical analysis in Supporting Information).

Applying the Arrhenius relation from equation (7) in

[14] with parameters from T_1 data of ^1H NMR and conductivity measurements, we determine the correlation time of protonic motion, τ_{NMR} , to be 330 ps at 525 K. This timescale falls between our computed slow (λ_2^{-1}) and productive (λ_3^{-1}) rotations. The productive rotation timescale also matches our observed 500 ps equilibration period for MD to enter the diffusive regime, highlighting the necessity of ML MD for probing such long-time dynamics.

The Arrhenius plot (Figure 4b) yields activation energies of 0.16 eV and 0.35 eV for fast (λ_1) and slow (λ_2) polyanion rotations, respectively, indicating distinct mechanisms. We extend the two-rate rotation model, previously observed in monoclinic CsH_2PO_4 via ^{17}O NMR [47], to the superprotonic phase. These findings establish two-rate rotation as an intrinsic characteristic of CsH_2PO_4 across both phases.

The activation barriers for slow (λ_2 , 0.35 eV) and productive (λ_3 , 0.36 eV) rotations are nearly identical, suggesting they share a rate-limiting step. The productive rotation barrier also approaches the activation energy derived from diffusion coefficients (0.43 eV, Figure 2), confirming that productive carrier rotations control long-range proton transport.

E. Population of bound protons on rotation rates

In CsH_2PO_4 , each PO_4 polyanion has two bound protons (i.e., protons that form O-H bonds) on average, twice that of SO_4 in CsHSO_4 . We hypothesize that these protons act as connectors between polyanions, with the higher proton content in CsH_2PO_4 frustrating polyanion rotations. This explains the distinct fast (λ_1) and slow (λ_2) rotation rates in CsH_2PO_4 , contrasting with the single rate in CsHSO_4 (Figure 7a).

To investigate how local proton coordination influences rotation rates, we analyze the bound protons surrounding polyanion pairs during residence time intervals (τ_{O-O}). Figure 4c shows a typical configuration where the residing proton H_r forms an O-H bond with the host polyanion (left) and an $\text{H}\cdots\text{O}$ hydrogen bond with the neighbor polyanion (right). We count bound protons ($N_p(t)$) on the neighbor polyanion using a mutual nearest-neighbor criterion, and calculate the time-averaged number $\bar{N}_p(\tau_{O-O})$:

$$\bar{N}_p(\tau_{O-O}) = \frac{1}{M} \sum_{t=t_i}^{t=t_i+\tau_{O-O}} N_p(t), \quad (3)$$

where t_i is the starting time and M is the number of MD snapshots within τ_{O-O} .

The probability density map of (\bar{N}_p, τ_{O-O}) (Figure 4d) reveals that shorter residence times ($\tau_{O-O} < \tau_c$) correlate with fewer bound protons ($\bar{N}_p \approx 1.8$) compared to longer times ($\bar{N}_p \approx 2.0$ for $\tau_{O-O} \geq \tau_c$). This temporary

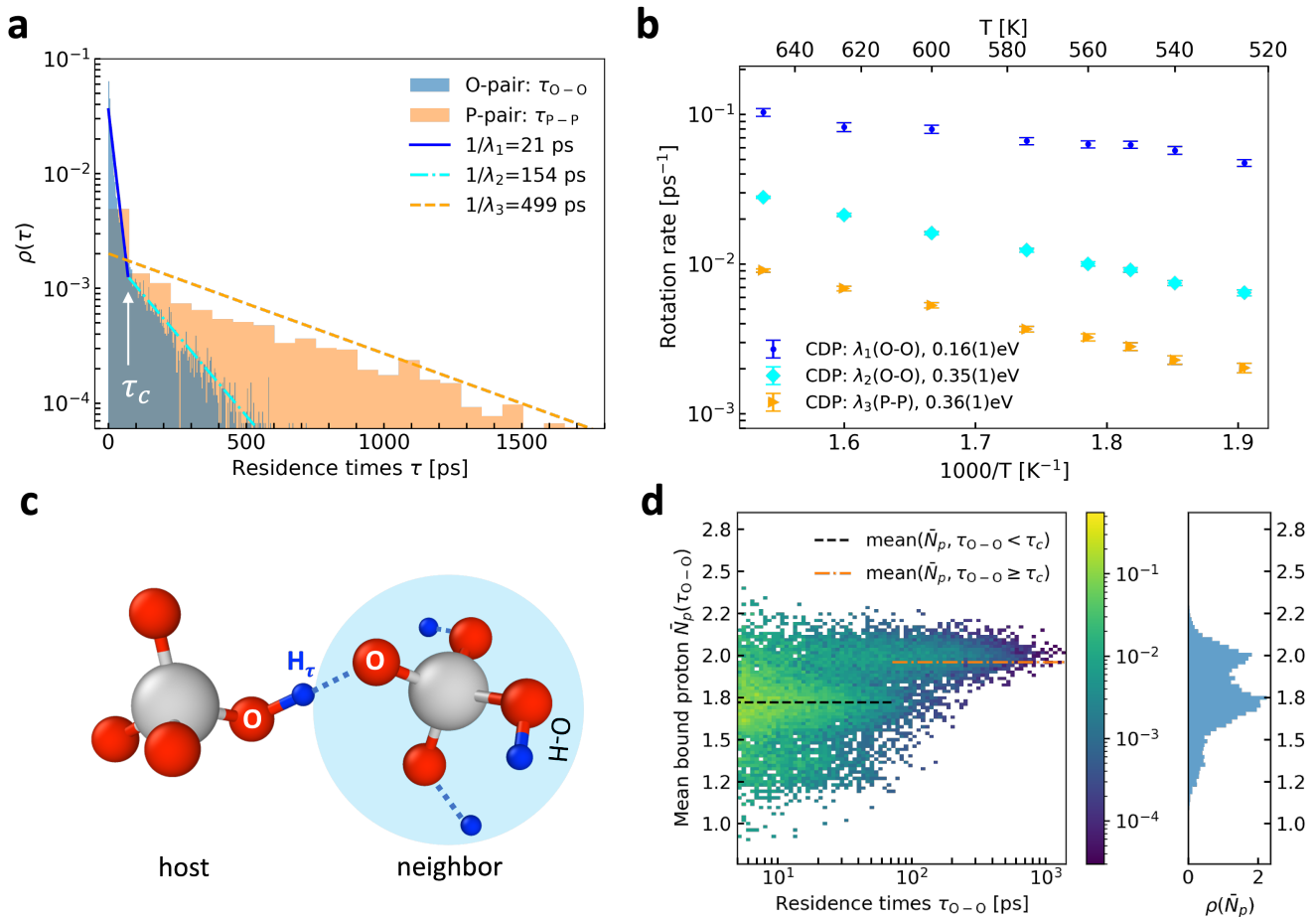


Figure 4. Two-rate behavior and effect of bound protons (a) Distribution of O-pair and P-pair residence times from all protons in a 4 ns ML MD simulation of CsH₂PO₄ at 525 K. O-pair residence times include intervals between both productive and nonproductive rotations, exhibiting fast (λ_1) and slow (λ_2) rates, while P-pair residence times encompass only intervals between productive rotations, occurring at rate λ_3 . τ_c marks the transition from fast to slow rotation. (b) Arrhenius plot of general rotation rates (λ_1 and λ_2) alongside the productive rotation rate (λ_3) across various temperatures. (c) Counting of bound protons (with O–H bond), $N_p(t)$, on the neighbor polyanion (right) at $t \in \tau_{O-O}$. A neighbor polyanion is defined as the one primarily forming the H_τ...O bond with its residing proton (H_τ) during τ_{O-O} . (d) Joint probability density of $\bar{N}_p(\tau_{O-O})$ and τ_{O-O} , where $\bar{N}_p(\tau_{O-O})$ is the time-averaged bound protons number on the neighbor polyanion as a function of τ_{O-O} . The color scale represents the magnitude of the joint probability. The marginal probability density of \bar{N}_p (right) reveals two distinct peaks in the population of bound protons attached on the neighbor polyanion in CsH₂PO₄.

reduction in bound protons lowers the rotational barrier, enabling faster (λ_1) rotations. The marginal probability of \bar{N}_p reveals two distinct peaks, reflecting significant local fluctuations in bound proton populations that create the dynamic environment that splits rotation rates in CsH₂PO₄.

F. O–H bond reorientation and slingshot migration

Previously, we established that polyanion rotation alone cannot explain the observed proton jump distances. To resolve this discrepancy, we investigate O–H bond reorientation during rotation periods. Figure 5a demonstrates how significant O–H reorientation on the carrier enables additional proton displacement toward the next PO₄ polyanion.

We quantify O–H reorientation during rotation period

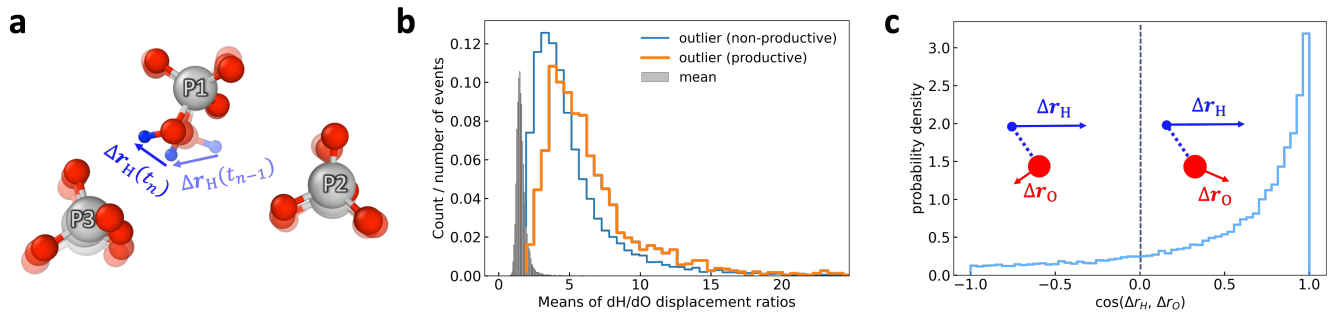


Figure 5. O–H bond reorientation (a) Three consecutive ML MD snapshots illustrating significant O–H bond reorientation occurring on the carrier P1, despite minimal rotation of the carrier itself at the moment. (b) Distributions of mean dH/dO ratios (defined in Eq. 4) for both productive and nonproductive rotations in CsH_2PO_4 , along with outlier distributions for each. (c) Distribution of cosine angles between instantaneous H and O displacements during all rotational motions, illustrating that most O–H reorientations extends proton displacement in the direction of the polyanion’s rotation.

$[t_s, t_f]$ using the dH/dO ratio:

$$\frac{\Delta r_{\text{H}}(t_n)}{\Delta r_{\text{O}}(t_n)} = \frac{|\mathbf{r}_{\text{H}}(t_n) - \mathbf{r}_{\text{H}}(t_{n-1})|}{|\mathbf{r}_{\text{O}}(t_n) - \mathbf{r}_{\text{O}}(t_{n-1})|}, \forall t_n, t_{n-1} \in [t_s, t_f] \quad (4)$$

where consecutive MD snapshots (t_n, t_{n-1}) are separated by 50 fs. This ratio measures instantaneous proton displacement relative to its bonded O anion, with a value of 1 indicating synchronized movement.

During rotation periods, dH/dO ratios typically fluctuate around 1, with occasional spikes indicating O–H reorientation events (Fig. S7, Supporting Information). For each period, we calculate a baseline **mean** ratio and an **outlier** value—the average of ratios with Z-scores exceeding 2—representing significant O–H reorientation events.

Analysis across all protons reveals three distributions (Fig. 5b): mean ratios peaking at 1.5 (baseline including thermal effects), and outlier distributions peaking at 3.6 and 4.1 for nonproductive and productive rotations, respectively. These higher outlier peaks indicate substantial “proton swings,” with greater magnitude in productive rotations. The clear separation between baseline and outlier distributions emphasizes these swings’ importance in rotation-assisted transport. These proton swings can act like a slingshot, enhancing proton displacement, especially when aligned with the polyanion rotation direction.

To verify the transport contribution of these reorientations, we analyze the alignment between proton and oxygen displacements through the cosine angle, $\cos(\Delta \mathbf{r}_{\text{H}}(t_n), \Delta \mathbf{r}_{\text{O}}(t_n))$ during rotation periods. Figure 5c shows predominantly aligned motions, leading us to term this the “proton slingshot” mechanism. This synergistic combination of productive carrier rotation and aligned O–H reorientation emerges as a crucial component of the long-range proton transfer mechanism.

G. Correlation of O-sharing and proton dynamics

Having established the importance of O–H reorientation in the proton transfer mechanism, we now examine a unique phenomenon in CsH_2PO_4 that further influences proton dynamics during polyanion rotations. This phenomenon arises from the high proton coordination per polyanion in this material.

In CsH_2PO_4 , the hydrogen-to-oxygen stoichiometry ensures each proton associates with a distinct O-pair. Our ML MD simulations confirm that dual proton occupation of a single O-pair is energetically prohibited, with zero instances observed. However, we observe O-sharing events, where a single O atom is simultaneously shared by two protons from different O-pairs (Figure 6b). At 525 K, an average of 12.8% of protons participate in such O-sharing configurations during at each MD step.

Figure 6a shows O-sharing during a productive rotation that precedes O–H bond reorientation and proton hopping. This suggests O-sharing creates local electrostatic repulsion that facilitates O–H reorientation and subsequent proton transfer between polyanions. To examine the correlation between O-sharing and proton dynamics, we monitor O-sharing events within each proton’s O-pair from 50 ps before rotation completion (t_f). The normalized distributions (Figure 6c) reveal that O-sharing probability doubles during both productive and nonproductive rotations, demonstrating its critical role in proton transport. O-sharing events decrease 1.4 ps and 0.6 ps before completing productive and nonproductive rotations, respectively. This decline corresponds to the formation of stable O–H...O configuration as the system approaches post-transfer equilibrium.

Notably, O-sharing is unique to CsH_2PO_4 , as no such configurations are observed in CsHSO_4 simulations.

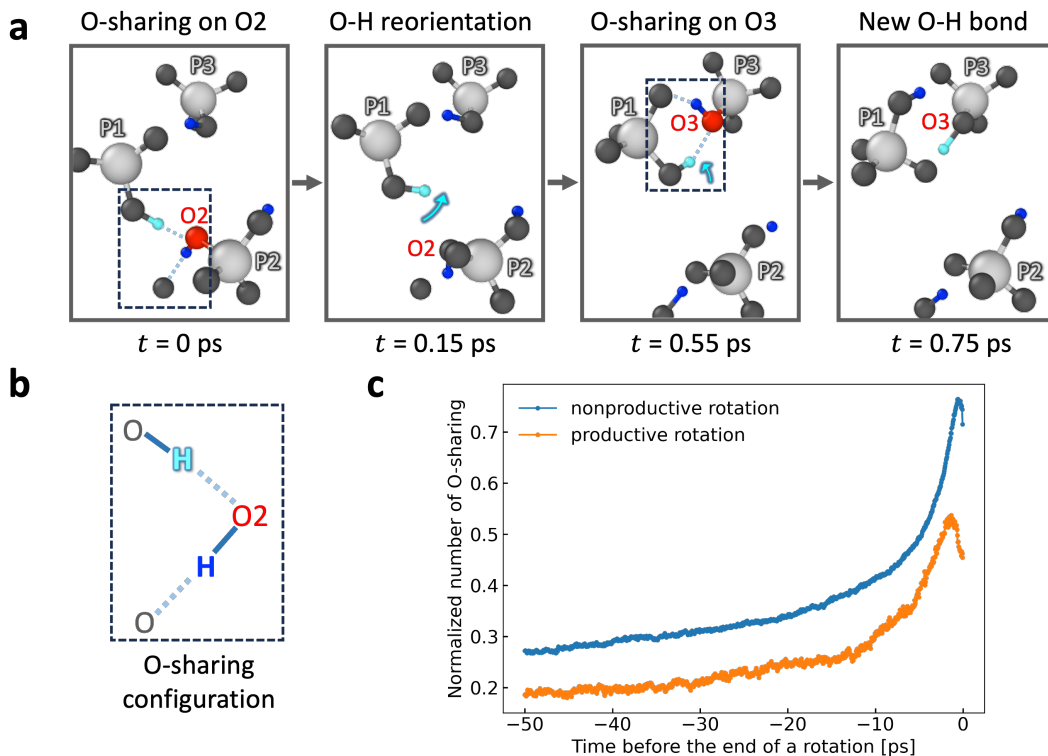


Figure 6. O-sharing (a) ML MD snapshots illustrating two O-sharing configurations during a productive carrier rotation. The configuration is boxed with shared O anion marked red. At 0 ps, the shared O2 repels the O–H bond, reorienting it away from provider P2. At 0.55 ps, carrier P1 brings the hopping proton (cyan) near O3 via rotation, creating another O-sharing configuration. At 0.75 ps, O3 offloads its previously bonded proton (blue) and receives the hopping proton by forming a new O–H bond. (b) Example of O-sharing, where O2 is shared by two protons. (c) Distribution of O-sharing events over time, normalized by the total number of productive or nonproductive rotations. The time is referenced from the end of each rotation (t_f). O-sharing occurrence increases significantly prior to both types of polyanion rotations.

This distinction highlights the unique proton bonding geometry in CsH_2PO_4 and its correlation with proton transport, driven by the compound’s higher proton concentration.

H. Local proton transfer in CsHSO_4

CsHSO_4 , like CsH_2PO_4 , is an exemplar solid acid compound that exhibits high proton conductivity with lower activation energy. Intriguingly, it achieves this despite having one less proton per polyanion group. Previous AIMD studies [12, 20] revealed faster polyanion rotations but slower local proton transfer in CsHSO_4 compared to CsH_2PO_4 . However, the underlying mechanism behind the faster SO_4 rotations remains unexplored due to the limited spatial scale of AIMD.

Several key questions arise from these observations: How does the reduced proton concentration in CsHSO_4 influence its polyanion dynamics? What are the critical

mechanistic differences between CsHSO_4 and CsH_2PO_4 that lead to their distinct behaviors? Can larger-scale simulations provide insights that AIMD studies have been unable to capture?

Understanding these aspects is crucial for elucidating the fundamental principles governing proton conduction in solid acids. To address these questions, we begin by investigating the local proton transfer behavior in CsHSO_4 from our MLMD simulations that allow for sufficient spatial and temporal scales.

Tracking the nearest O anion to a proton (Figure S9, Supporting Information) reveals less frequent proton rattling within O-pairs in CsHSO_4 , with an average timescale of 1.9 ps at 500 K, compared to 0.27 ps at 525 K in CsH_2PO_4 . This suggests a deeper double-well potential energy landscape for protons within O-pairs in CsHSO_4 , inhibiting rapid local proton transfer.

In CsHSO_4 , the completion of productive rotations, marked by new O–H bond formation with recipient polyanions, occurs after significant proton displacement.

This delayed completion arises because protons first reach toward recipient polyanions to form O–H...O bonds before breaking their O–H bonds with carrier polyanions, resulting in delayed SO₄ polyanion pair (S-pair) switches.

I. Polyanion rotation and O–H reorientation in CsHSO₄

We examine the coupling between polyanion and proton dynamics in CsHSO₄ using the analysis technique from section III D. We estimate the general polyanion rotation rate from the O-pair residence time distribution and the productive rotation rate from the S-pair residence times. Figure 7a reveals that, unlike the two-rate behavior in CsH₂PO₄, CsHSO₄ exhibits a single-rate behavior for polyanion rotations. Productive rotations in CsHSO₄ at 450 K occurs about four times faster than CsH₂PO₄ at 525 K. Notably, in both compounds, the timescale of productive rotations matches with that of equilibrated proton diffusion, indicating that productive polyanion rotations are closely coupled to long-range proton diffusion.

Analysis of CsHSO₄ reveals a single peak in bound proton population ($\bar{N}_p(\tau_{O-O}) = 1$, Figure 7b), consistent with its single-rate rotation and previous observations that proton bonding minimally affects polyanion dynamics [48]. This contrasts with CsH₂PO₄'s two-peak distribution arising from its higher proton content. The Arrhenius plot (Figure 7c) shows identical fast (λ_1) rotation barriers of 0.16 eV in both compounds, suggesting less hindrance from surrounding bound protons. However, CsH₂PO₄'s additional proton introduces local population fluctuations that create higher activation barriers for slow rotations (λ_2). As a result of fewer proton-polyanion constraints, CsHSO₄ exhibits faster productive rotations (λ_3), consistent with its higher proton mobility in ML MD simulations (Figure 2b).

Significant O–H reorientation also occurs in CsHSO₄ during rotations, as indicated in Figure 7d, further supporting the proton slingshot mechanism. The mean dH/dO ratios peak around 1.4, while outlier distributions reach 5.2 in productive rotations and 3.7 in nonproductive ones. The direction of O–H reorientation aligns with the carrier rotation (Figure S8, Supporting Information), highlighting its role in facilitating proton jumps. These findings confirm Baranov's hypothesis [1] and align with NMR experimental observations [49] of new H inter-bond motion in superprotonic CsHSO₄. Our large-scale ML MD simulations validate the occurrence of significant O–H reorientation during long-range proton jumps in both CsH₂PO₄ and CsHSO₄, establishing this as a common mechanism in superprotonic solid acids.

J. Polyanion orientations in CsHSO₄ and CsH₂PO₄

We further distinguish SO₄ and PO₄ dynamics by analyzing their preferred orientations and the timescale required to explore the orientation space.

We characterize each XO₄ polyanion (X = S or P) orientation using a single X–O bond vector, defined by azimuthal and polar angles (Figure 8a). Tracking this vector for a randomly selected polyanion over 4 ns yields cumulative orientation distributions shown in Figure 8b,c. SO₄ exhibits distinct peaks, indicating preferences for specific orientations, while PO₄ shows a more disordered distribution due to frustrated polyanion interactions via bound protons.

This orientational difference is further supported by the probability distributions of full orientation space presented in Figure 8e,f (details in Supporting Information). SO₄ orientations in CsHSO₄ display clear, well-defined peaks that align with experimental oxygen sites (marked by red crosses), while PO₄ orientations in CsH₂PO₄ show broader, flatter distribution peaks around experimental orientations.

The contrast in orientational behavior can be attributed to the varying proton concentrations in the two compounds. The higher proton concentration around PO₄ in CsH₂PO₄ imposes stronger rotational constraints, leading to more frustrated polyanion interactions and greater orientational disorder. Conversely, the lower proton concentration surrounding SO₄ in CsHSO₄ results in weaker rotational constraints, allowing for more distinct orientations.

To compare the rates at which SO₄ and PO₄ polyanions decouple from a given orientation, we compute the time-window averaged vector autocorrelation function (VCF) [12, 13]:

$$\text{VCF}(\Delta t) = \frac{1}{M} \frac{1}{N} \sum_{t=0}^{T-\Delta t} \sum_{i=1}^N \mathbf{a}_i(t) \cdot \mathbf{a}_i(t + \Delta t). \quad (5)$$

where $\mathbf{a}_i(t)$ is the unit X–O vector for the i -th polyanion at time t , M is the number of time windows with duration Δt , N is the number of XO₄ polyanions, and T is the total time considered in the calculation.

Figure 8d shows that the S–O bond decays below 0.5 at 17 ps, while the P–O bond takes 114 ps at the same simulation temperature, indicating significantly faster SO₄ rotations. This analysis further emphasizes the impact of proton concentration on polyanion dynamics in these superprotonic solid acids, with the lower proton concentration in CsHSO₄ allowing for faster and more defined rotations compared to CsH₂PO₄.

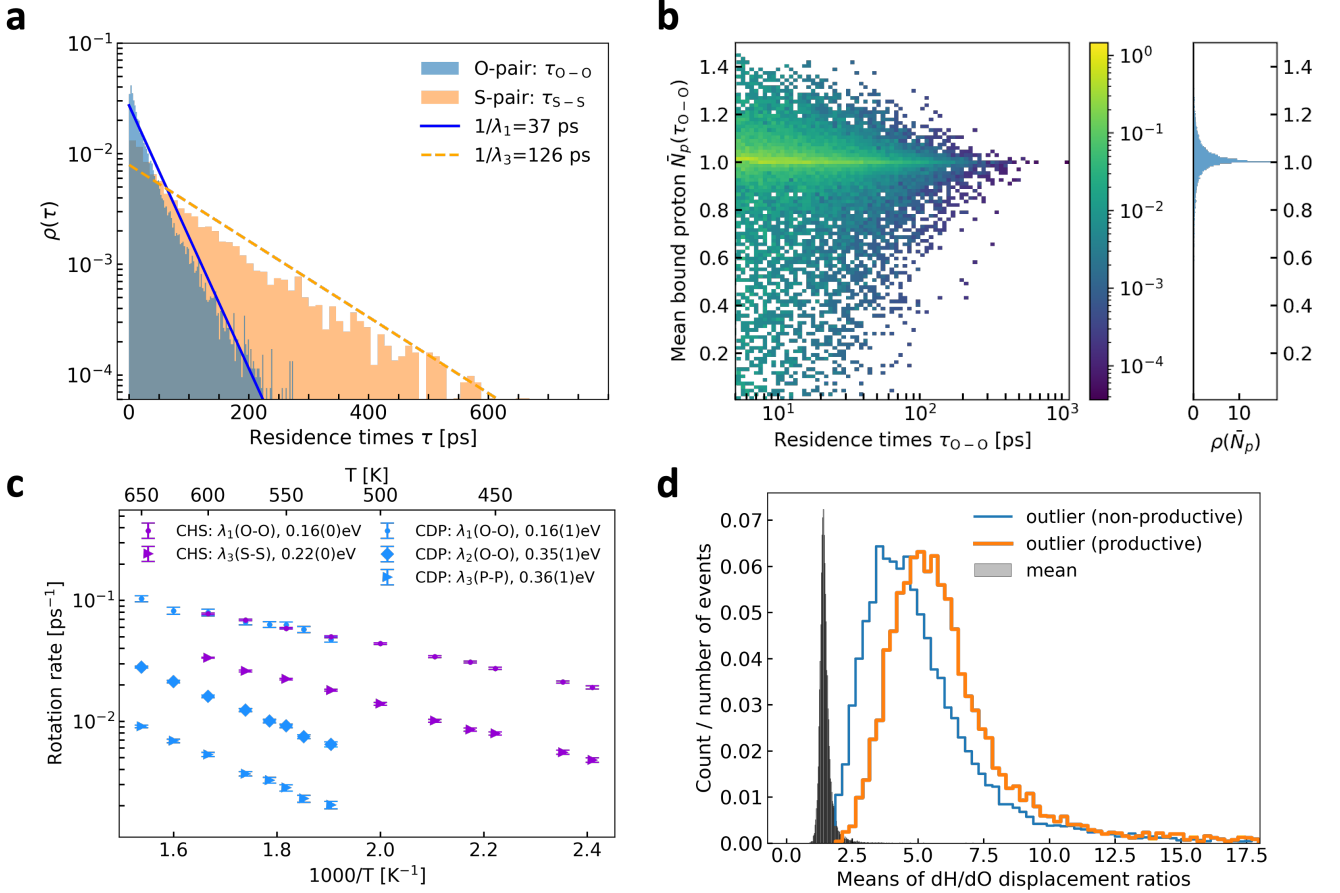


Figure 7. Proton slingshot mechanism in CsHSO₄ (a) Residence time distributions from a 4ns ML MD simulation of CsHSO₄ at 450 K. Both O-pair and S-pair residence time distributions indicate a single-rate polyanion rotation. (b) Joint probability density of $\bar{N}_p(\tau_{O-O})$ and τ_{O-O} at 450 K with marginal probability of \bar{N}_p (right) suggests a single peak in the population of bound protons on the neighbor polyanion of CsHSO₄. (c) Arrhenius plot of general polyanion rotation rates (λ_1, λ_2) and productive rotation rates (λ_3) in CsHSO₄ and CsH₂PO₄. (d) Distributions of mean dH/dO ratios from both rotation types, along with outlier distributions for each in CsHSO₄.

IV. CONCLUSION

Our study unveils a new paradigm for understanding proton transport in solid acid compounds, specifically CsH₂PO₄ and CsHSO₄. We reveal a proton slingshot mechanism, where cooperative motion between small scale polyanion rotation and significant O-H bond reorientation facilitates long-range proton transfer. This challenges the conventional revolving paddlewheel model and provides a more nuanced understanding of the transport process.

We identify two distinct types of polyanion rotations: productive carrier rotations contributing to long-range proton diffusion, and nonproductive exchanger rotations. The activation barriers for productive rotations closely align with those of proton diffusion, underscoring their critical role in high proton mobility.

Our work elucidates the impact of proton concentration on rotational dynamics, explaining the observed differences between CsH₂PO₄ and CsHSO₄. The higher proton content in CsH₂PO₄ leads to two-rate rotations and increased rotational frustration, contrasting with the single-rate, faster rotations in CsHSO₄. This insight suggests that reducing proton concentration could potentially enhance conductivity by alleviating rotational frustration.

The extended spatial and temporal scales of our ML-accelerated MD simulations, combined with our novel analysis techniques, provide access to the full picture of proton transport in these materials. This approach offers a powerful framework for characterizing proton and polyanion dynamics in solid acid compounds, opening new avenues for identifying and optimizing superprotonic conductors.

Our findings not only bridge the gap between

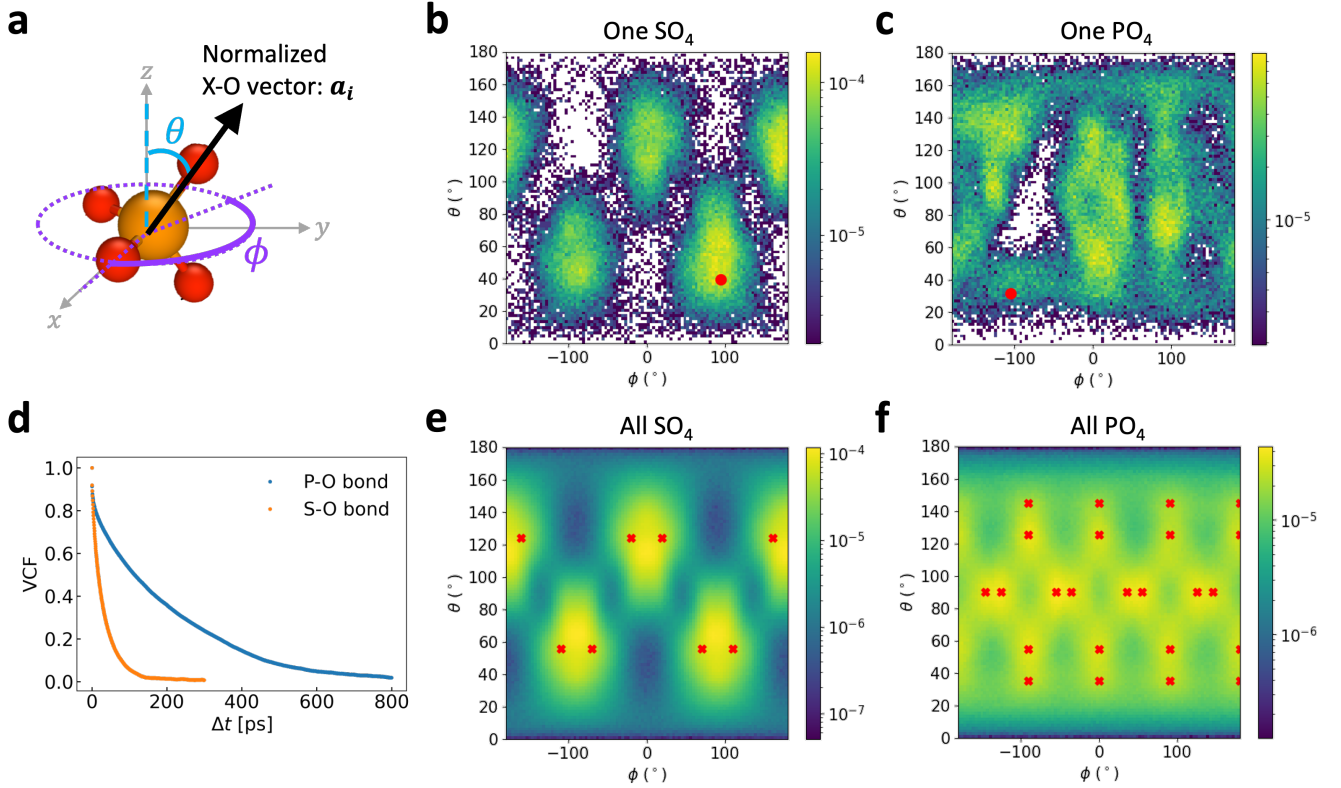


Figure 8. Polyanion orientations in CsHSO_4 and CsH_2PO_4 **a** Illustration of a normalized X–O vector in an XO_4 polyanion and its spherical angles (ϕ, θ). Cumulative probability distribution of the spherical angles of a single X–O vector in one selected polyanion for **b** CsHSO_4 and **c** CsH_2PO_4 from their respective 4 ns ML MDs at 550 K. Each red dot indicates the initial spherical angles of the tracked X–O bond. **d** VCF calculated by Eq. 5 for CsHSO_4 and CsH_2PO_4 from 4 ns ML MDs at 550K. Cumulative distribution of the spherical angles of the X–O bond with the minimum initial θ from all polyanions for **e** CsHSO_4 and **f** CsH_2PO_4 . Red crosses denote experimental oxygen sites [15, 21]. SO_4 polyanions exhibit more distinct and well-defined orientations compared to PO_4 polyanions.

polyanion rotation and proton transport but also provide insights for materials design. By establishing the link between local proton coordination, polyanion rotation, and long-range transport, we offer a unified framework for understanding and enhancing proton conductivity in solid acid compounds, potentially accelerating the development of next-generation fuel cells and energy storage devices.

V. DATA AVAILABILITY

The *ab initio* dataset of CsH_2PO_4 and CsHSO_4 generated from this study will be provided on the Zenodo platform via <https://zenodo.org/uploads/14649023> upon publication.

VI. CODE AVAILABILITY

The analysis tools and implementation details will be made publicly available upon publication of this article. Open-source software implementations of FLARE and Allegro are available at <https://github.com/mir-group/flare> and <https://github.com/mir-group/allegro>, git commit e5dcd1953168fee056970fa7dd86294c3d1f437f.

VII. REFERENCES

-
- [1] Baranov, A. I. *Crystallography Reports* **2003**, *48*, 1012–1037.
- [2] Haile, S. M.; Boysen, D. A.; Chisholm, C. R. I.; Merle, R. B. *Nature* **2001**, *410*, 910–913.
- [3] Boysen, D. A.; Uda, T.; Chisholm, C. R. I.; Haile, S. M. *Science* **2004**, *303*, 68–70.
- [4] Merle, R. B.; Chisholm, C. R. I.; Boysen, D. A.; Haile, S. M. *Energy and Fuels* **2002**, *17*, 210–215.
- [5] Gittleman, C. S.; Jia, H.; Castro, E. S. D.; Chisholm, C. R.; Kim, Y. S. *Joule* **2021**, *5*, 1660–1677.
- [6] Papandrew, A. B.; Wilson, D. L.; M. Cantillo, N.; Hawks, S.; Atkinson, R. W.; Goenaga, G. A.; Zawodzinski, T. A. *Journal of The Electrochemical Society* **2014**, *161*, F679–F685.
- [7] Lim, D.-K.; Plymill, A. B.; Paik, H.; Qian, X.; Zecevic, S.; Chisholm, C. R.; Haile, S. M. *Joule* **2020**, *4*, 2338–2347.
- [8] A. I. Baranov, N. M. S., L. A. Shuvalov *JETP Letter* **1982**, *36*, 459–462.
- [9] Baranov, A. I.; Khiznichenko, V. P.; Sandler, V. A.; Shuvalov, L. A. *Ferroelectrics* **1988**, *81*, 183–186.
- [10] Kreuer, K.-D. *Chemistry of Materials* **1996**, *8*, 610–641.
- [11] Norby, T. *Solid State Ionics* **1999**, *125*, 1–11.
- [12] Drefler, C.; Sebastiani, D. *Physical Chemistry Chemical Physics* **2020**, *22*, 10738–10752.
- [13] Jinnouchi, R. *Physical Chemistry Chemical Physics* **2022**, *24*, 15522–15531.
- [14] Ishikawa, A.; Maekawa, H.; Yamamura, T.; Kawakita, Y.; Shibata, K.; Kawai, M. *Solid State Ionics* **2008**, *179*, 2345–2349.
- [15] Yamada, K.; Sagara, T.; Yamane, Y.; Ohki, H.; Okuda, T. *Solid State Ionics* **2004**, *175*, 557–562.
- [16] Blinc, R. *Solid State Ionics* **1995**, *77*, 97–100.
- [17] Belushkin, A. V.; Carlile, C. J.; Shuvalov, L. A. *Journal of Physics: Condensed Matter* **1992**, *4*, 389–398.
- [18] Badot, J.; Colomban, P. *Solid State Ionics* **1989**, *35*, 143–149.
- [19] Wood, B. C.; Marzari, N. *Physical Review B* **2007**, *76*, 134301.
- [20] Lee, H.-S.; Tuckerman, M. E. *The Journal of Physical Chemistry C* **2008**, *112*, 9917–9930.
- [21] Jirak, Z.; Dlouha, M.; Vratislav, S.; Balagurov, A. M.; Beskrovnyi, A.; Gordelii, V.; Datt, I.; Shuvalov, L. *Physica Status Solidi A, Applied Research* **1987**, *100*, 117–122.
- [22] Wang, L. S.; Patel, S. V.; Sanghvi, S. S.; Hu, Y.-Y.; Haile, S. M. *Journal of the American Chemical Society* **2020**, *142*, 19992–20001.
- [23] Drefler, C.; Hänseroth, J.; Sebastiani, D. *The Journal of Physical Chemistry Letters* **2023**, *14*, 7249–7255.
- [24] Behler, J.; Parrinello, M. *Physical Review Letters* **2007**, *98*, 146401.
- [25] Vandermause, J.; Xie, Y.; Lim, J. S.; Owen, C. J.; Kozinsky, B. *Nature Communications* **2022**, *13*.
- [26] Xie, Y.; Vandermause, J.; Ramakers, S.; Protik, N. H.; Johansson, A.; Kozinsky, B. *npj Computational Materials* **2023**, *9*.
- [27] Batzner, S.; Musaelian, A.; Sun, L.; Geiger, M.; Mailoa, J. P.; Kornbluth, M.; Molinari, N.; Smidt, T. E.; Kozinsky, B. *Nature Communications* **2022**, *13*.
- [28] Musaelian, A.; Batzner, S.; Johansson, A.; Sun, L.; Owen, C. J.; Kornbluth, M.; Kozinsky, B. *Nature Communications* **2023**, *14*.
- [29] Minami, S.; Jinnouchi, R. *Journal of Materials Chemistry A* **2023**, *11*, 16104–16114.
- [30] Vandermause, J.; Torrisi, S. B.; Batzner, S.; Xie, Y.; Sun, L.; Kolpak, A. M.; Kozinsky, B. *npj Computational Materials* **2020**, *6*.
- [31] Haile, S. M.; Chisholm, C. R. I.; Sasaki, K.; Boysen, D. A.; Uda, T. *Faraday Discuss.* **2007**, *134*, 17–39.
- [32] Shigenobu Hayashi, M. M. *Solid State Ionics* **2004**, *171*, 289–293.
- [33] Perdew, J. P.; Burke, K.; Ernzerhof, M. *Physical Review Letters* **1996**, *77*, 3865–3868.
- [34] Troeye, B. V.; van Setten, M. J.; Giantomassi, M.; Torrent, M.; Rignanese, G.-M.; Gonze, X. *Physical Review B* **2017**, *95*, 024112.
- [35] Krzystyniak, M.; Druzbicki, K.; Fernandez-Alonso, F. *Physical Chemistry Chemical Physics* **2015**, *17*, 31287–31296.
- [36] Parker, S. F.; Cavaye, H.; Callear, S. K. *Molecules* **2020**, *25*, 1271.
- [37] Saßnick, H.-D.; Cocchi, C. *Electronic Structure* **2021**, *3*, 027001.
- [38] Kresse, G.; Furthmüller, J. *Computational Materials Science* **1996**, *6*, 15–50.
- [39] Kresse, G.; Furthmüller, J. *Physical Review B* **1996**, *54*, 11169–11186.
- [40] Kresse, G.; Joubert, D. *Physical Review B* **1999**, *59*, 1758–1775.
- [41] Drautz, R. *Physical Review B* **2019**, *99*, 014104.
- [42] Fu, X.; Wu, Z.; Wang, W.; Xie, T.; Keten, S.; Gomez-Bombarelli, R.; Jaakkola, T. *Transactions on Machine Learning Research, 2023* **2022**.
- [43] Kingma, D. P.; Ba, J. *ArXiv e-prints* **2014**.
- [44] Paszke, A.; et al. *ArXiv e-prints* **2019**.
- [45] Thompson, A. P.; Aktulga, H. M.; Berger, R.; Bolintineanu, D. S.; Brown, W. M.; Crozier, P. S.; in ’t Veld, P. J.; Kohlmeyer, A.; Moore, S. G.; Nguyen, T. D.; Shan, R.; Stevens, M. J.; Tranchida, J.; Trott, C.; Plimpton, S. J. *Computer Physics Communications* **2022**, *271*, 108171.
- [46] Aili, D.; Gao, Y.; Han, J.; Li, Q. *Solid State Ionics* **2017**, *306*, 13–19.
- [47] Kim, G.; Griffin, J. M.; Blanc, F.; Haile, S. M.; Grey, C. P. *Journal of the American Chemical Society* **2015**, *137*, 3867–3876.
- [48] Münch, W.; Kreuer, K.; Traub, U.; Maier, J. *Solid State Ionics* **1995**, *77*, 10–14.
- [49] Arcon, D.; Blinc, R.; Dolinsek, J.; Shuvalov, L. A. *Physical Review B* **1997**, *55*, 8961–8966.
- [50] Stukowski, A. *Modelling and Simulation in Materials Science and Engineering* **2009**, *18*, 015012.

VIII. ACKNOWLEDGEMENTS

The authors gratefully acknowledge Kyle Bystrom for insightful discussions on DFT calculations, Anders Johansson for suggesting the residence time approach

and guidance on using LAMMPS, and Gordon Peiker for providing feedback on the manuscript figures. The authors also thank Jenny Hoffman and Suzanne Smith for their editing feedback on the initial version of the manuscript. This work was primarily supported by National Science Foundation, Office of Advanced Cyberinfrastructure (OAC), under Award No. 2118201. M.W., G.X., N.Z., R.P.A, S.H., and B.K. were supported by National Science Foundation, OAC, under Award No. 2118201. J.D. was supported by the National Science Foundation under Grant No. DMR-2119351. C.J.O was supported by the U.S. Department of Energy, Office of Science, Office of Basic Energy Sciences, Chemical Sciences, Geosciences, and Biosciences Division under Award Number DE-SC0022199. A.M. and B.K. were supported by Harvard University Materials Research Science and Engineering Center under Grant No. DMR-2011754. Y.X was supported by the National Science Foundation under Grant No. OAC-2003725. N.M. was supported by Bosch Research. The authors acknowledge computing resources provided by the Harvard University FAS Division of Science Research Computing Group. The analysis and visualization of MD simulations were conducted using OVITO software [50].

IX. AUTHOR CONTRIBUTIONS

M.W. generated the datasets, trained and validated MLFFs, conducted ML MD simulations, implemented data analysis codes, created the figures, and wrote the manuscript. J.D. provided mentorship, suggested analysis ideas, revised the manuscript and figures, and provided the MSD calculation code. G.X. contributed the experimental crystal structures of CsH_2PO_4 , provided measured conductivity data, and feedback on data analysis. N.Z. contributed code for analyzing polyanion rotation. C.J.O. guided M.W. in DFT and FLARE calculations and gave feedback on data analysis. Y.X. provided suggestions and support on using FLARE. A.M. offered suggestions and support on Allegro model training. N.M. provided the example code to obtain diffusion coefficients and feedback on proton trajectory analysis. B.K., S.H, and R.P.A. supervised the project and guided the analysis of simulations. All authors contributed to the manuscript.

X. COMPETING INTERESTS

The authors declare no competing interests.

Supporting Information for:

Revealing the proton slingshot mechanism in solid acid electrolytes through machine learning molecular dynamics

Menghang Wang¹, Jingxuan Ding¹, Grace Xiong², Ni Zhan³, Cameron J. Owen⁴, Albert Musaelian¹, Yu Xie¹, Nicola Molinari^{1,5}, Ryan P. Adams³, Sossina Haile², and Boris Kozinsky^{1,5,*}

¹Harvard John A. Paulson School of Engineering and Applied Sciences, Harvard University, Cambridge, MA 02138, USA

²Materials Science and Engineering, Northwestern University, Evanston, IL 60208, USA

³Department of Computer Science, Princeton University, Princeton, NJ 08544, USA

⁴Department of Chemistry and Chemical Biology, Harvard University, Cambridge, MA 02138, USA

⁵Robert Bosch Research and Technology Center, Watertown, MA 02472, USA

Contents

1	H position in CsH ₂ PO ₄	3
2	DFT calculation	3
3	Dataset generation	3
4	MLFF validation	4
5	MLMD setup	4
6	Diffusion coefficients and error estimation	6
7	MSD of CsHSO ₄	7
8	Residence time analysis	7
9	Categorized residence time distribution	8
10	Rotation period	9
11	Overlaps between nonproductive and productive rotations	9

12 dH/dO ratios over a pair switch duration	10
13 O–H bond reorientation	11
14 Proton trajectory of CsHSO ₄	11
15 SO ₄ orientations	12

1 H position in CsH₂PO₄

For CsH₂PO₄, there are no experimental reports of hydrogen positions in the literature. Therefore, we use the geometry proposed in [1] to position H atoms in the cubic CsH₂PO₄ as the starting structure. Based on Fig. 6 in [1], the following assumptions were made: the P, O, and H atoms are on the same z -plane, the P–O–H angle is 110°, and the O–H intra-phosphate group distance is 1.02 Å. The other atomic coordinates (Cs, P, O) were sourced from experimentally derived data in [2]. For an O atom at (0.2299, 0.6270, 0.5), the calculated position of the H atom is (0.3002, 0.8202, 0.5).

2 DFT calculation

We utilized plane wave basis sets and projector augmented wave (PAW) in our calculations, with a plane wave cut-off energy set at 700 eV for both CsH₂PO₄ and CsHSO₄. The convergence criterion for the electron self-consistent loop, EDIFF, was set to 10⁻⁵. Given that both CsH₂PO₄ and CsHSO₄ are insulators, Gaussian smearing with a width of 0.1 eV was applied. In addition, LASPH was enabled to include non-spherical contributions in the PAW spheres.

The Monkhorst-Pack scheme was applied for Brillouin zone sampling. For the superprotonic phase (Pm $\bar{3}$ m) of CsH₂PO₄, the cubic unit cell [3] contains one formula unit with a lattice parameter of 4.95 Å. We utilized a 2 × 2 × 2 k -point mesh for both the 2 × 2 × 2 supercell (64 atoms) and the 3 × 3 × 3 supercell (144 atoms). For the monoclinic CsH₂PO₄ (P2₁/m), the unit cell [4] contains two formula units with lattice parameters: $a = 7.91$ Å, $b = 6.38$ Å, $c = 4.88$ Å. We used a 2 × 2 × 2 k -point mesh for the 2 × 2 × 2 supercell (128 atoms). Superprotonic CsHSO₄ (I4₁/amd) has a unit cell [5] with four formula units and lattice parameters: $a, b = 5.72$ Å, $c = 14.23$ Å. Both monoclinic phases (III and II, both with symmetry of P2₁/c) of CsHSO₄ have four formula units each. Phase III [6] has $a = 8.21$ Å, $b = 5.81$ Å, $c = 10.98$ Å, while phase II [7] has $a = 7.80$ Å, $b = 8.21$ Å, $c = 8.04$ Å. We used a 2 × 2 × 2 k -point mesh for the 2 × 2 × 1 supercell (112 atoms) for all three phases.

3 Dataset generation

Starting structures of superprotonic phases were generated using `OrderDisorderedStructureTransformation` from `pymatgen` [8], selecting configurations with proper tetrahedral PO₄ and SO₄ geometries. Internal atomic positions were optimized using VASP (ISIF = 2) while maintaining cell parameters, with Cs and P positions additionally constrained for superprotonic CsH₂PO₄. Monoclinic phase structures of both compounds were fully relaxed using VASP (ISIF = 3).

Table S1 summarizes the active learning trajectory setup. Each trajectory began with an empty SGP model to maximize diverse atomic environment sampling while avoiding initial data bias and preventing SGP slowdown as the dataset expands. Data collection ends when DFT calls reduce to approximately 1 per 1000 MD steps, ensuring comprehensive sampling of high-uncertainty environments. Simulations were conducted above 800 K to enhance configuration diversity through increased kinetic contributions. We employed different stress

tensor constraints in LAMMPS NpT simulations (triclinic "tri" and anisotropic "aniso") to capture varied cell-symmetry effects. The ACE B2 descriptor [9] was configured with a body order of five and varied radial cutoffs. Radial distribution function analysis confirmed that sampled structures remained physically realistic, free from decomposition, melting, or unrealistic bond lengths.

For CsH_2PO_4 , we collected 1,196 MD snapshots spanning 300-1,000 K, incorporating both superprotonic ($\text{Pm}\bar{3}\text{m}$) and monoclinic ($\text{P}2_1/\text{m}$) phases with system size of 64, 128, and 144 atoms. The CsHSO_4 dataset comprises 1,636 MD snapshots from 200-2,000 K, covering superprotonic ($\text{I}4_1/\text{amd}$) and monoclinic (III and II) phases.

4 MLFF validation

The root mean square error (RMSE) on forces from test sets are $45 \text{ meV}/\text{\AA}$ for CsH_2PO_4 with 130 MD snapshots and for $114 \text{ meV}/\text{\AA}$ for CsHSO_4 with 199 MD snapshots. The comparisons between the DFT forces and ML forces of all components are shown in Figure S1.

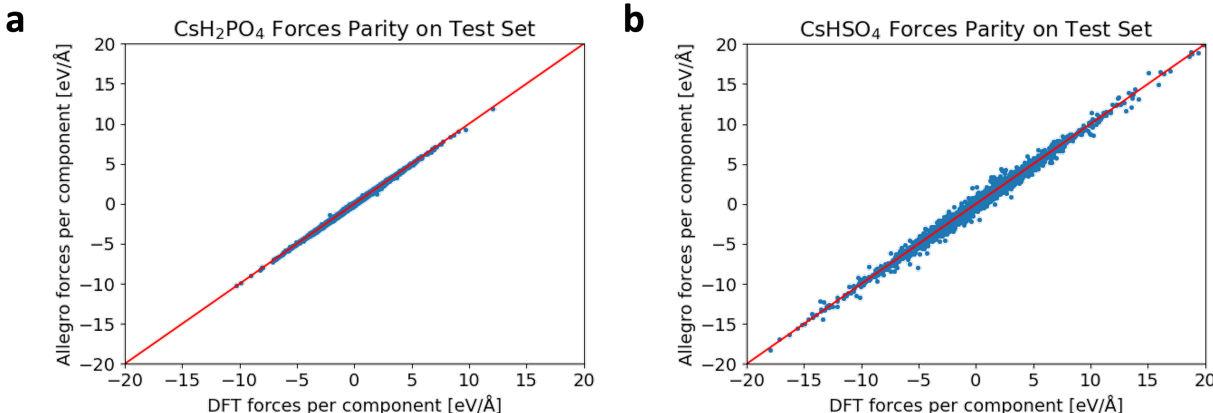


Figure S1. Force parity plot on the test set of (a) CsH_2PO_4 and (a) CsHSO_4 , respectively.

In our equation-of-states test on CsH_2PO_4 and CsHSO_4 , we obtain the structures of their superprotonic phases from the final frame of 100 ps NVT AIMD simulations (144 atoms at 525 K for CsH_2PO_4 , and 112 atoms at 500 K for CsHSO_4), which are not included in the training data. We isotropically scale cell parameters to compare energies predicted by Allegro with those calculated via DFT (PBE). As shown in Figure S2, Allegro's energy predictions align with DFT within $2 \text{ meV}/\text{atom}$ for lattice parameter scaling from 0.92 to 1.08 in CsH_2PO_4 and 0.94 to 1.10 for CsHSO_4 . The predictive error is defined as $(E_{\text{Allegro}} - E_{\text{PBE}})/N_{\text{atoms}}$, with N_{atoms} being the number of atoms in the cell.

5 MLMD setup

For CsH_2PO_4 , we run simulations for 4 ns at temperatures of 525, 540, 550, 560, and 575 K, and for 3 ns at temperatures at 600, 625, and 650 K. For CsHSO_4 , we run simulations for

Phase	Temp.	Press.	Ensemble	N_{atoms}	r_c	N_{DFT}
CsH ₂ PO ₄ (P2 ₁ /m)	300	1	NPT (aniso)	128	5.5	21
	400	1	NPT (aniso)	128	5.5	23
	500	1	NPT (aniso)	128	5.5	64
CsH ₂ PO ₄ (Pm $\bar{3}$ m)	600	1	NPT (aniso)	144	5.5	91
	800	1	NPT (aniso)	144	5.5	102
	1000	1	NPT (aniso)	144	5.5	94
	525	1	NPT (tri)	64	5.5	139
	600	1	NPT (aniso)	64	5.5	115
	700	1	NPT (tri)	64	5.5	55
	800	1	NPT (aniso)	64	5.5	167
	1000	1	NPT (tri)	64	5.5	90
	1000	1	NPT (tri)	64	5.5	235
CsHSO ₄ (P2 ₁ /c, III)	200	0	NPT (tri)	112	5.5	36
	300	0	NPT (tri)	112	5.5	35
	300	1	NPT (tri)	112	5.5	39
	300	1.2e4	NPT (tri)	112	4.0	12
	300 to 600	0	NPT (tri)	112	5.5	66
	400	0	NPT (tri)	112	5.5	37
	500	0	NPT (tri)	112	5.5	54
	800	0	NPT (tri)	112	5.5	85
CsHSO ₄ (P2 ₁ /c, II)	360	1	NPT (tri)	112	4.0	21
	360	1.2e4	NPT (tri)	112	4.0	17
	400	1	NPT (aniso)	112	5.5	26
	500	1	NPT (tri)	112	5.5	47
	800	1	NPT (tri)	112	5.5	95
	800	1	NPT (aniso)	112	5.5	36
CsHSO ₄ (I4 ₁ /amd, I)	450	0	NPT (tri)	112	5.5	181
	450 to 300	0	NPT (iso)	112	5.5	84
	800	0	NPT (tri)	112	5.5	104
CsHSO ₄ (I4 ₁ /amd, I)	450	0	NPT (tri)	112	5.5	48
	550	0	NPT (tri)	112	5.5	37
	550	0	NPT (aniso)	112	5.5	32
	550	1	NPT (aniso+tri)	112	5.5	55
	800	0	NPT (tri)	112	5.5	54
	2000	0	NPT (aniso+tri)	112	5.5	80
	800	1	NPT (tri)	112	6.6	165
	2000	1	NPT (tri)	112	6.0	190

Table S1. Setup details and dataset information from FLARE Bayesian active learning workflow [10, 11, 12]: the material phase; simulation temperature (K); pressure (Bar); statistical ensemble; number of atoms N_{atoms} in the simulation cell; radial cutoff r_c (Å) of the ACE descriptor; number of collected MD snapshots N_{DFT} with DFT-calculated labels.

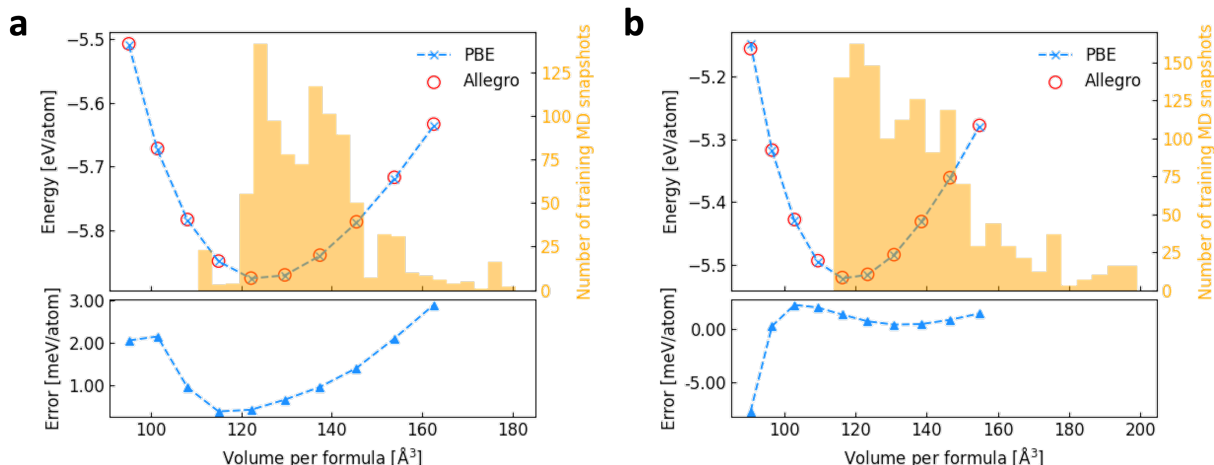


Figure S2. Energy-volume curves for the superprotonic phases of **(a)** CsH_2PO_4 (144 atoms, 525 K) and **(b)** CsHSO_4 (112 atoms, 500 K) from a snapshot of corresponding NVT AIMD simulations. Data are predicted by the Allegro model (circles) and DFT calculations with PBE functional (crosses). Predictive errors remain within 2 meV/atom for lattice parameter 0.92 to 1.08 for CsH_2PO_4 and 0.94 to 1.10 for CsHSO_4 . The orange histogram illustrates the training data distribution relative to volume per formula unit.

4 ns at temperatures at 415, 425, 450, 460, 475, 500, 525, 550, 575, and 600 K.

We use the same experimental lattice parameters across different temperatures and ignore the effect of lattice expansion.

6 Diffusion coefficients and error estimation

To obtain the proton diffusion coefficient (D), we fit the slope of the proton MSD in the diffusive regime according to the Einstein equation. The MSD is computed with time window averaging [13], and the curve is truncated at 70% of the total simulation time to mitigate poor statistics from a few long time-windows. We estimate the slope using a fitting window with $\tau \geq 1$ ns.

For CsH_2PO_4 , we estimate the standard deviation of the fitted diffusion coefficients at selected temperatures using N number of independent ML MD simulations. Each simulation used a different velocity random seed but began with the same initial structure. In the table below, Temp. refers to the temperature of the ML MD simulation, N represents the number of independent trajectories, and std. dev. is the standard deviation of diffusion coefficients across these trajectories. Notably, the standard deviation is an order of magnitude smaller than the calculated diffusion coefficients.

Temp. (K)	N	std. dev. (cm^2/s)
525	5	1.013×10^{-8}
550	10	2.023×10^{-8}
575	5	2.642×10^{-8}

7 MSD of CsHSO₄

Fig. S3 illustrates the significance of long-timescale MD simulations in examining proton and polyanion dynamics in CsHSO₄.

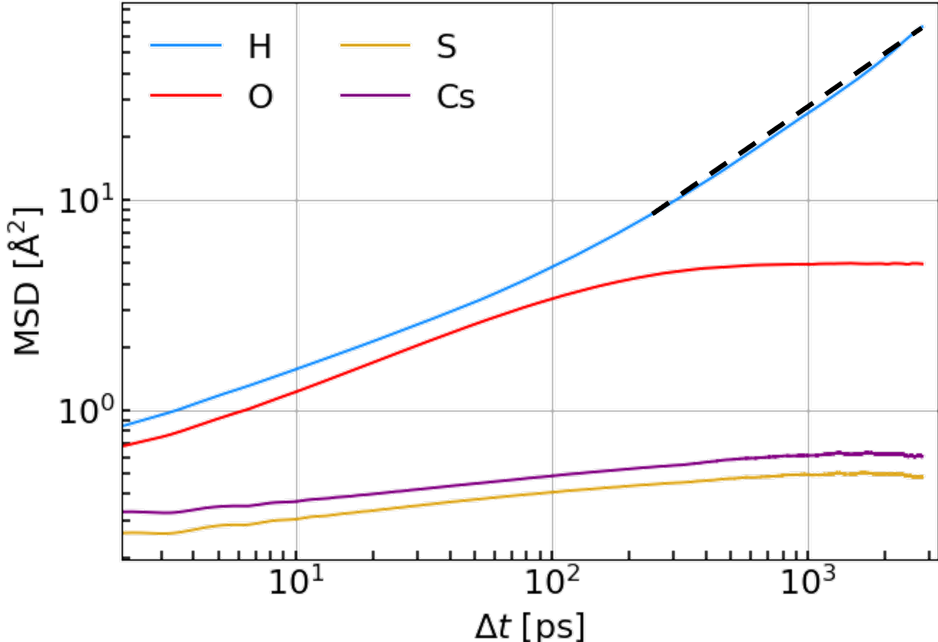


Figure S3. MSDs of each species in CsHSO₄ from a 4 ns ML MD at 450 K. Proton diffusive regime starts at 200 ps, and the oxygen MSD plateaus around 500 ps.

8 Residence time analysis

We collect the residence time from each proton trajectory and exclude the intervals bounded by either the start or the end of the simulation, which artificially terminates a proton residency. To ensure a robust rate fitting and accurately represent the probability density function, we determine the optimal histogram bin size using the Freedman–Diaconis rule. Furthermore, we enhance the model’s resilience to outliers by excluding regions with extremely low probability density, specifically considering only probability density ($\rho(\tau)$) above 2×10^{-4} for O-pair and 5×10^{-5} for P-pair residence times.

To identify the transition point τ_c , we minimize the difference in R^2 values between segments before and after τ_c , as shown in Eq. 1, while scanning the values of τ_c increasingly.

$$R^2(\tau < \tau_c) - R^2(\tau \geq \tau_c) \tag{1}$$

We then use `curve_fit()` from `scipy.optimize` [14] to fit a piecewise linear function

with four parameters (k_1, k_2, τ_c, b_1) to the residence time distribution ($\tau, \log(\rho)$):

$$\begin{cases} k_1\tau + b_1 & \tau < \tau_c \\ k_2(\tau - \tau_c) + k_1\tau_c + b_1 & \tau \geq \tau_c \end{cases} \quad (2)$$

where k_1 is the fast rate, k_2 is the slow rate, and b_1 is the vertical intercept with $\log(\rho)$. This approach accurately estimates the transition point τ_c , distinguishing between fast and slow rotations.

9 Categorized residence time distribution

An O-pair residence time, representing the interval between two consecutive rotation events of a given proton, can be categorized based on the type of each rotation event. For instance, a residence time between a nonproductive and a productive rotation, regardless of their order, is denoted as (nonproductive-productive). In addition, O-pair residence times separated by two consecutive productive rotations represent only a subset of P-pair residence times (τ_{P-P}) on shorter timescales. P-pair residence times also include intervals separated by two consecutive P-pair switches with nonproductive rotations occurring in between. The categorized O-pair residence times are shown in Figure S4, revealing that the two-rate rotation behavior is inherent across all types of rotations.

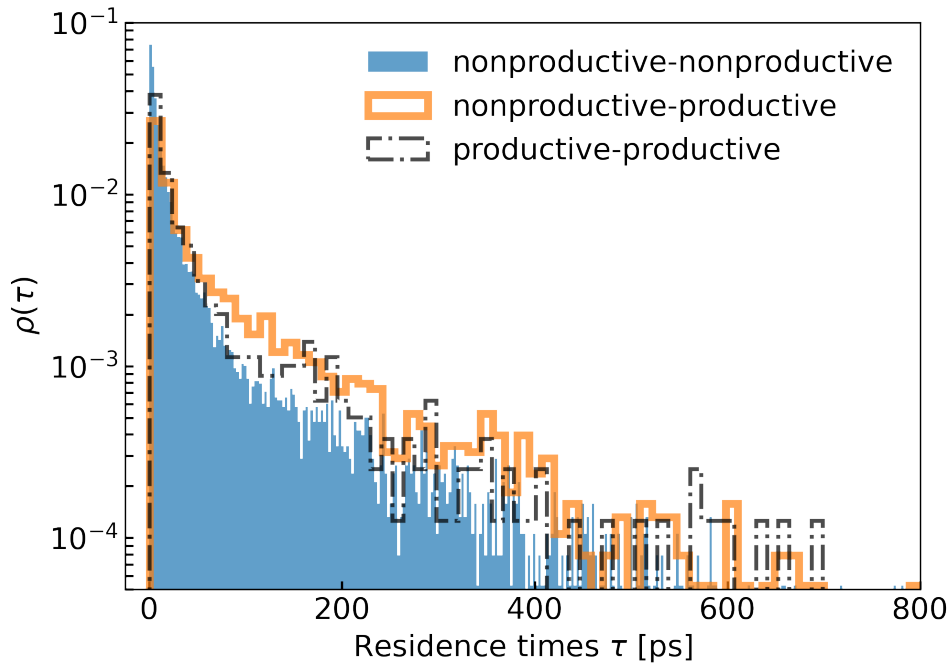


Figure S4. O-pair residence times distribution at 525 K in CsH_2PO_4 categorized into the intervals separated by two nonproductive rotations (nonproductive-nonproductive), one nonproductive rotation and one productive rotation (nonproductive-productive), and two productive rotations (productive-productive).

10 Rotation period

Figure S5 and Figure S6 show the rotation period length distributions for CsH_2PO_4 and CsHSO_4 from ML MD simulations. In CsH_2PO_4 , average rotation periods for O-pair and P-pair switches are 2.4 ps and 3.9 ps, respectively. CsHSO_4 exhibits longer periods (15.8 ps and 24.5 ps) due to slower O–H bond breaking. In both compounds, these timescales are significantly shorter than intervals between pair switch events. The x-axes are truncated at the 99th percentile for clarity. Despite differing timescales, these observations support treating polyanion rotation as a discrete event in both materials. For clarity, the x-axes in both figures are truncated at the 99th percentile to focus on the most representative data. Despite different timescales between the two compounds, these observations support treating polyanion rotation as a discrete event rather than an extended process in both cases.

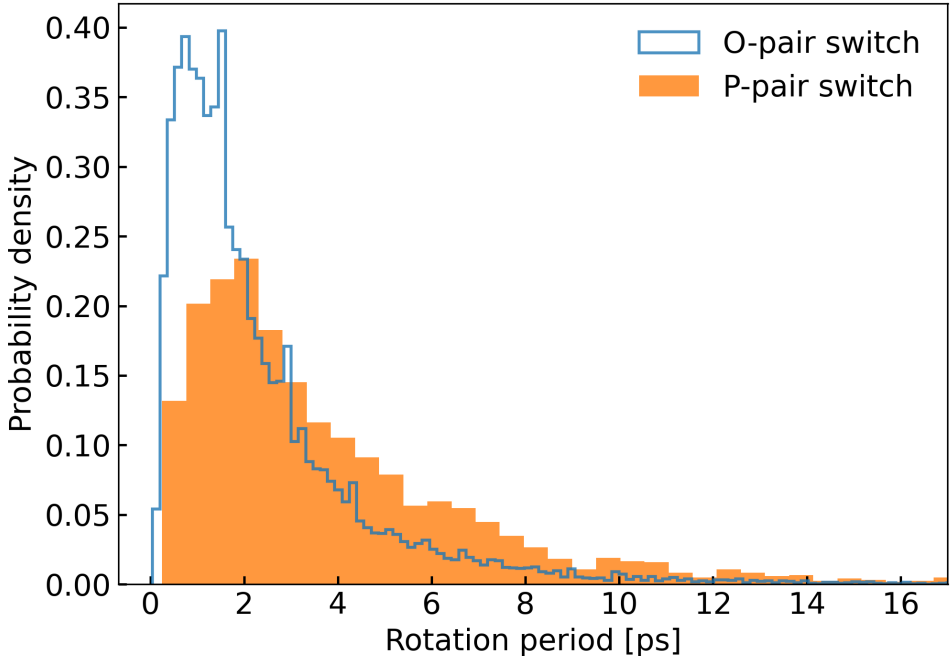


Figure S5. Distribution of polyanion rotation periods in CsH_2PO_4 at 525 K.

11 Overlaps between nonproductive and productive rotations

In each rotation, the rotation period from t_s to t_f is assigned to each relevant polyanion: the carrier and exchanger in nonproductive rotations, and the provider, carrier, and recipient in productive ones. Consequently, a polyanion accumulates sets of nonproductive, $\{(t_{s,N}, t_{f,N})\}$, and productive rotation durations, $\{(t_{s,P}, t_{f,P})\}$.

To determine overlap between these rotations, we apply the following criteria:

$$t_{s,N} \leq t_{s,P} \leq t_{f,N} \text{ or } t_{s,N} \leq t_{f,P} \leq t_{f,N}. \tag{3}$$

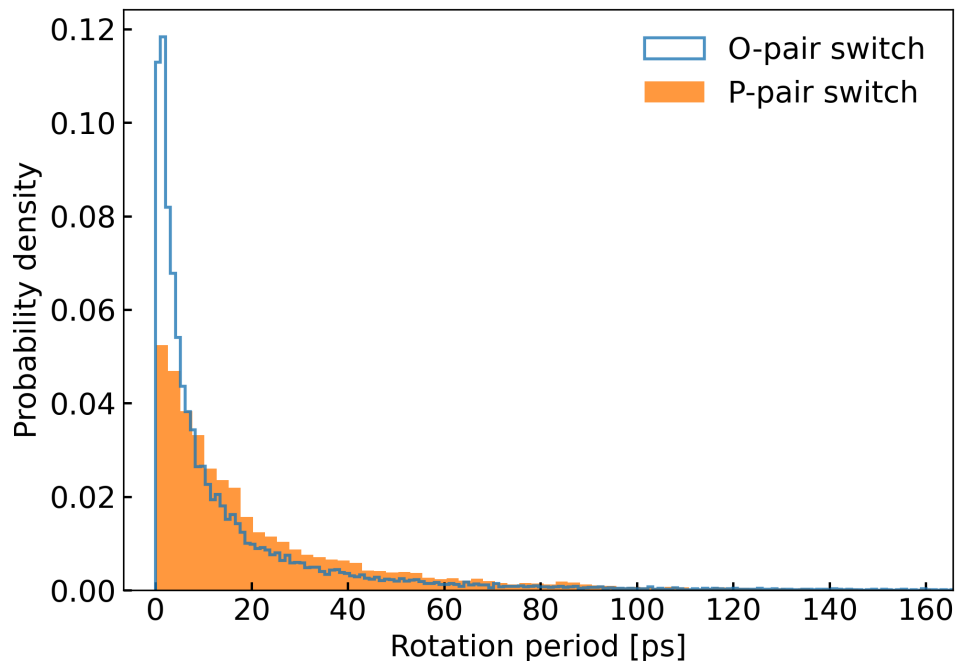


Figure S6. Distribution of polyanion rotation periods in CsHSO₄ at 450 K.

Table S2 reveals the overlap, indicating that when a polyanion acts as an exchanger or carrier in a nonproductive rotation, there may be overlap with times it serves as provider, carrier, or recipient in productive rotations. This method provides an upper bound on overlap estimates, as it considers entire rotational intervals rather than just the endpoints of P-pair switch events, which would yield significantly fewer overlaps.

Role in a nonproductive rotation	Role in a productive rotation	No overlap	1 overlap	2 overlaps
exchanger	carrier	99.33%	0.67%	0%
exchanger	recipient	94.20%	5.76%	0.04%
exchanger	provider	94.67%	5.24%	0.09%
carrier	carrier	98.90%	1.10%	0%
carrier	recipient	98.27%	1.73%	0%
carrier	provider	98.00%	1.98%	0.02%

Table S2. Overlaps between nonproductive and productive rotations.

12 dH/dO ratios over a pair switch duration

Figure S7 shows the time evolution of dH/dO ratios of a single proton during one of its polyanion rotation periods. For each period, we obtain (1) a **mean** of all dH/dO ratios as a baseline (2) an **outlier** value, capturing significant O–H reorientation.

This approach offers a more precise indicator of O–H reorientation than the angular difference method between consecutive MD snapshots. The latter can falsely indicate reorientation when only the oxygen anion moves without the O–H bond swinging. For instance, a rotating P–O bond with a fixed P–O–H angle would show an angular difference of O–H bonds between MD snapshots, despite no actual O–H reorientation occurring.

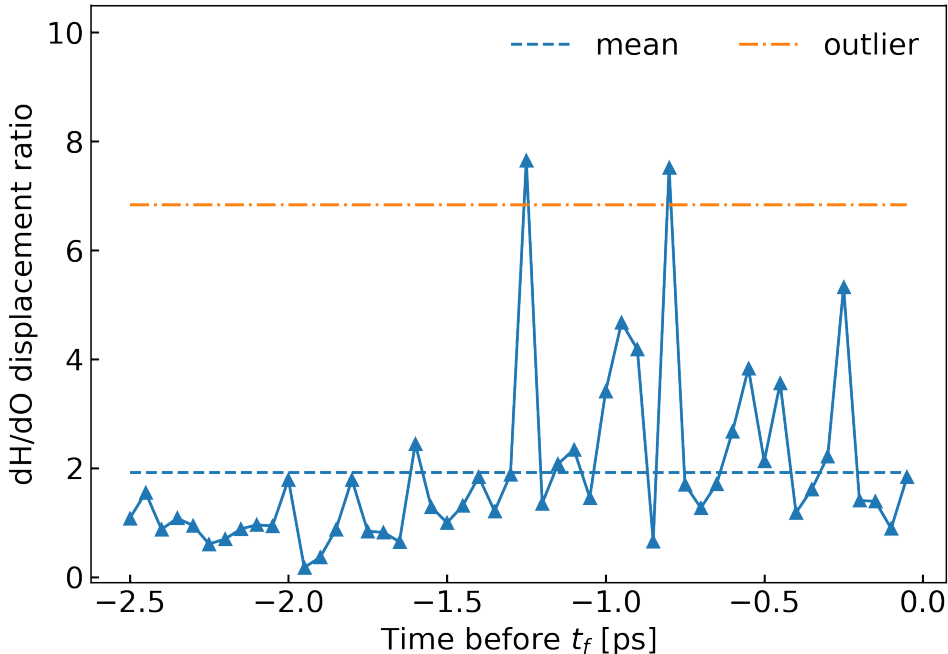


Figure S7. Evolution of dH/dO ratios, defined as $\Delta r_{\text{H}}(t_n)/\Delta r_{\text{O}}(t_n)$ for $t_n \in [t_s, t_f]$, tracked for a single proton during its polyanion rotation period. The blue dashed line represents the **mean** of all dH/dO ratios over this rotation period. The orange dot-dashed line indicates the **outlier**, calculated as the average of ratios with Z -scores greater than 2, highlighting significant O–H bond reorientation events.

13 O–H bond reorientation

Figure S8 demonstrates that in both CsHSO_4 and CsH_2PO_4 , the hopping proton predominantly moves in the direction of carrier rotation.

14 Proton trajectory of CsHSO_4

Figure S9 shows that protons in CsHSO_4 tend to bond more persistently with a single O anion, resulting in a slower rattling rate compared to CsH_2PO_4 . The red dashed lines indicate S-pair switch events, which occur following proton displacement jumps, as this involves the additional step of breaking the O–H bond.

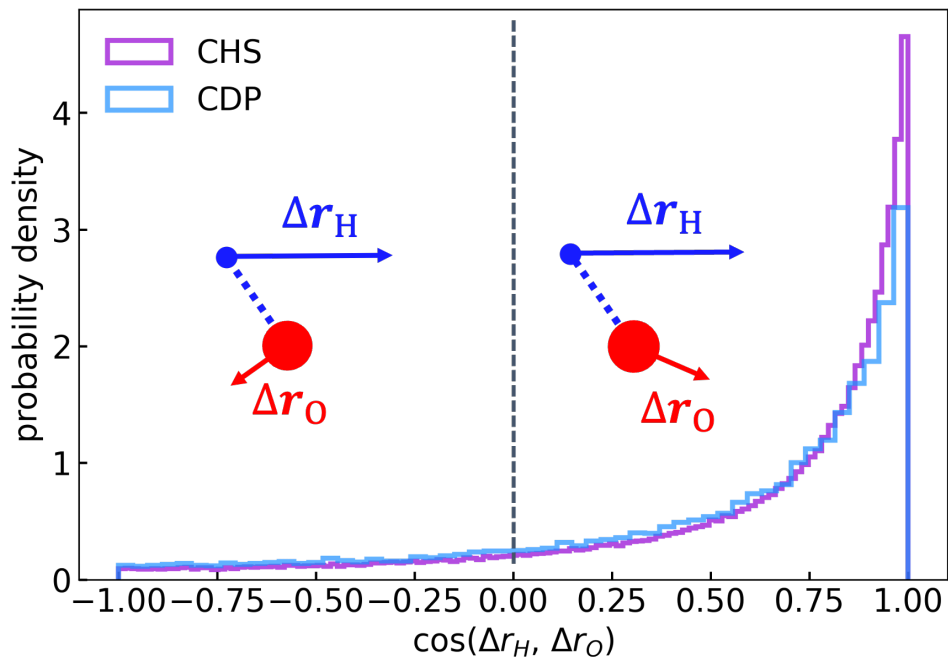


Figure S8. The distribution of cosine angles between the instantaneous H displacement and the instantaneous O displacement, defined as $\cos(\Delta\mathbf{r}_H(t_n), \Delta\mathbf{r}_O(t_n))$, during polyanion rotation period.

15 SO_4 orientations

In superprotonic CsHSO_4 , SO_4 tetrahedra alternate orientations along the c-axis. We apply symmetry operations to align these tetrahedra to a common reference frame, enabling direct comparison of polyanion orientations at later time.

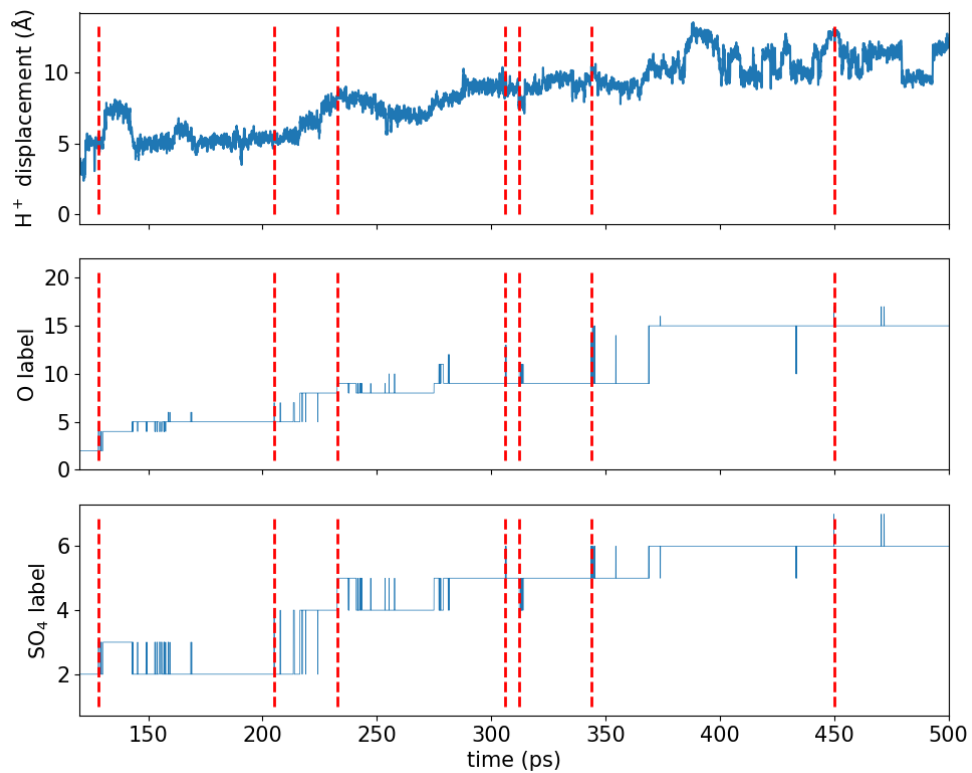


Figure S9. From top to bottom: the proton displacement, its nearest O anion, and its nearest SO₄ polyanion from a ML MD simulation of CsHSO₄ at 500 K.

Supplementary References

- [1] Lee, H.-S.; Tuckerman, M. E. *The Journal of Physical Chemistry C* **2008**, *112*, 9917–9930.
- [2] Botez, C. E.; Hermosillo, J. D.; Zhang, J.; Qian, J.; Zhao, Y.; Majzlan, J.; Chianelli, R. R.; Pantea, C. *The Journal of Chemical Physics* **2007**, *127*.
- [3] Yamada, K.; Sagara, T.; Yamane, Y.; Ohki, H.; Okuda, T. *Solid State Ionics* **2004**, *175*, 557–562.
- [4] Preisinger, A.; Mereiter, K.; Bronowska, W. In *European Powder Diffraction 3*; Trans Tech Publications Ltd; Materials Science Forum, Vol. 166; pp 511–516.
- [5] Jirak, Z.; Dlouha, M.; Vratislav, S.; Balagurov, A. M.; Beskrovnyi, A.; Gordelii, V.; Datt, I.; Shuvalov, L. *Physica Status Solidi A, Applied Research* **1987**, *100*, 117–122.
- [6] Chisholm, C. R.; Haile, S. M. *Materials Research Bulletin* **2000**, *35*, 999–1005.
- [7] Itoh, K.; Ukeda, T.; Ozaki, T.; Nakamura, E. *Acta Crystallographica Section C Crystal Structure Communications* **1990**, *46*, 358–361.
- [8] Ong, S. P.; Richards, W. D.; Jain, A.; Hautier, G.; Kocher, M.; Cholia, S.; Gunter, D.; Chevrier, V. L.; Persson, K. A.; Ceder, G. *Computational Materials Science* **2013**, *68*, 314–319.
- [9] Drautz, R. *Physical Review B* **2019**, *99*, 014104.
- [10] Vandermause, J.; Torrisi, S. B.; Batzner, S.; Xie, Y.; Sun, L.; Kolpak, A. M.; Kozinsky, B. *npj Computational Materials* **2020**, *6*.
- [11] Vandermause, J.; Xie, Y.; Lim, J. S.; Owen, C. J.; Kozinsky, B. *Nature Communications* **2022**, *13*.
- [12] Xie, Y.; Vandermause, J.; Ramakers, S.; Protik, N. H.; Johansson, A.; Kozinsky, B. *npj Computational Materials* **2023**, *9*.
- [13] He, X.; Zhu, Y.; Epstein, A.; Mo, Y. *npj Computational Materials* **2018**, *4*.
- [14] Virtanen, P.; et al. *Nature Methods* **2020**, *17*, 261–272.